Spring 4-22-2022

BINARY TRANSITION METAL OXIDES@REDUCED GRAPHENE OXIDE@POLYANILINE AS BIFUNCTIONAL ELECTRODE MATERIALS FOR ENERGY CONVERSION AND STORAGE

Jonghyun Choi
Pittsburg State University, jonghyun.choi@gus.pittstate.edu

BINARY TRANSITION METAL OXIDES@REDUCED GRAPHENE OXIDE@POLYANILINE AS BIFUNCTIONAL ELECTRODE MATERIALS FOR ENERGY CONVERSION AND STORAGE

A Thesis Submitted to the Graduate School
in Partial Fulfillment of the Requirements
For the Degree of
Master of Polymer Chemistry

Jonghyun Choi

Pittsburg State University

Pittsburg, Kansas

May, 2022

BINARY TRANSITION METAL OXIDES@REDUCED GRAPHENE OXIDE@POLYANILINE AS BIFUNCTIONAL ELECTRODE MATERIALS FOR ENERGY CONVERSION AND STORAGE

Jonghyun Choi

APPROVED:

Thesis Advisor _____
Dr. Ram Gupta, Department of Chemistry

Committee Member _____
Dr. Charles Neef, Department of Chemistry

Committee Member _____
Dr. Timothy Dawsey, Kansas Polymer Research Center

Committee Member _____
Dr. John Franklin, Department of English and Modern Languages

Acknowledgments

Firstly, I would like to express my gratitude to Dr. Ram Gupta. In 2018, when I was an undergraduate exchange student at Pittsburg State University, he encouraged me to apply to the master's program in Materials Science, and after I completed the MS in Materials Science, he suggested Polymer Chemistry program as a second major. Furthermore, Dr. Gupta supervised my hands-on training in various techniques and equipment in the laboratory, as well as generously offering his electrochemistry and polymer expertise. Thus, while I was pursuing my dual degrees for nearly three years, I learned an immense amount and expanded my knowledge rapidly. Again, I would like to say thank you to him.

Secondly, I convey my gratitude to Polymer Chemistry program advisor Dr. Khamis Siam. He helped me to select good courses to fit my interests and needs. In addition, he encouraged me and gave me sincere advice for my next step after graduation.

Thirdly, I would like to say thank you to Dr. Peter R. Dvornic, Dr. Jeanne Norton, and Dr. Paul Herring. They provided great lectures with their passion and effort. As a result, I learned a great deal about polymer science and technology.

Fourthly, I would also like to extend my appreciation to my committee members: Dr. Charles Neef, Dr. Tim Dawsey, and Dr. John Franklin. Their advice and suggestions about my thesis enabled me to write a better thesis. Despite their busy schedules, they made time to support my academic efforts, and I thank them for sharing their precious insight.

Fifthly, I would like to thank Dr. Sanjay R. Mishra and their group. Thanks to their

help, I was able to achieve high quality SEM and XPS images of my materials. It helped me to improve the quality of my work.

Sixthly, I would like to give my thanks to my coworkers: Camila Zequine, Tenzin Ingsel, Seongwoo Hong, Muhammad Rizwan Sulaiman, Felipe M de Souza, Wang Lin, Prashant Kote, Sudhakar Reddy Madhira, Rishabh Srivastava, Shiva Bhardwaj, and Sahil Kumar Chaudhary. I enjoyed working with them.

Finally, I appreciate my family. They prayed and supported me to successfully finish the Polymer Chemistry degree. I sincerely thank them for what they have done for me.

BINARY TRANSITION METAL OXIDES@REDUCED GRAPHENE OXIDE@POLYANILINE AS BIFUNCTIONAL ELECTRODE MATERIALS FOR ENERGY CONVERSION AND STORAGE

An Abstract of the Thesis by
Jonghyun Choi

The world's increasing consumption of energy has led researchers to focus on research and development for high performance-energy devices. Development of materials used in energy devices is currently focused on improving the performance and stability of devices. Composite materials are well known as an effective way to improve the performance of an energy device. A composite is a combination of two or more materials with different properties, and such combinations can be of great help in advancing the performance of a composite material by adding the advantages or compensating for the disadvantages of each material.

In this study, ternary composite materials were synthesized by combining binary transition metal oxide (nickel cobalt oxide, nickel manganese oxide, manganese cobalt oxide) with reduced graphene oxide (rGO) and polyaniline (PANI). All ternary composite materials were prepared via successive employment of hydrothermal technique and polymerization of aniline. All materials were utilized as an electrode material for electrocatalysts and supercapacitor devices.

Ternary composite materials showed high activity towards oxygen evolution reaction, requiring low overpotential of 342, 340, 382 mV, and high electrocatalytic properties for hydrogen evolution reaction, achieving low overpotential of 134, 95, 117 mV for rGO/nickel cobalt oxide/ PANI, rGO/nickel manganese oxide/ PANI, and rGO/manganese cobalt oxide/PANI, respectively to reach a current density of 10

mA/cm^2. Also, ternary composite materials showed a specific capacitance ranging from 145-285 F/g at a scan rate of 2 mV/s, along with high capacitance retention and coulombic efficiency up to 7,000 charge/discharge cycles.

Consequently, the results suggest that a ternary composite material has the potential to be efficiently used with a bifunctional purpose as an energy conversion and storage application material.

TABLE OF CONTENTS

LIST OF TABLES

LIST OF FIGURES

CHAPTER I

INTRODUCTION

1.1 Need for energy

The global energy crisis and related environmental issues significantly affect our ecosystems, public human health, and economy. Without proper action, it will continue to negatively affect certain aspects of our everyday lives (e.g., increase of oil prices, health complications due to environmental pollution). In order to tackle these challenging issues, efficient energy devices are required. Electrocatalyst for water splitting and supercapacitor devices are known as advanced devices for energy conversion and storage, respectively.

1.2 Introduction of electrocatalyst for water splitting

Hydrogen is an important energy source. It is mainly utilized to produce ammonia for fertilizer and to refine petroleum [1]. In addition, a large amount of hydrogen is employed for fuel cell electric vehicles, which have recently attracted much attention as alternatives to internal combustion vehicles that pollute our environment. However, free hydrogen is present in only trace amounts on Earth; thus, hydrogen must be refined from other sources. Three methods are mainly used: (1) steam methane reforming, (2)

coal gasification, and (3) water electrolysis. Hydrogen can be achieved by the following reaction [1]:

(1) Steam methane reforming $CH_4 + 2H_2O \rightarrow 4H_2 + CO_2$

(2) Coal gasification $C + 2H_2O \rightarrow 2H_2 + CO_2$

(3) Water electrolysis $2H_2O \rightarrow 2H_2 + O_2$

Steam methane reforming and coal gasification methods account for more than 95% of hydrogen production, while water electrolysis accounts for only for 4%. Steam methane reforming and coal gasification seem efficient for clean energy production. However, both processes simultaneously contribute to environmental pollution due to the emission of CO_2. Therefore, many studies on water electrolysis methods that do not generate CO_2 are being conducted.

At the same time, the water electrolysis method is also effective for oxygen generation. Oxygen gas, in particular, is in higher demand and more necessary during this COVID-dominated era. Many COVID patients experience low oxygen levels, which can continue to drop if left unaddressed. The oxygen generated by water electrolysis can be stored for use in hospitals. Also, oxygen production from water is essential for the storage mechanism of the metal air battery, which is currently called the next generation battery. A commercial Li-ion battery shows an energy density of 200-250 Wh/kg, whereas a Li-air battery can deliver an energy density of 5,200 Wh/kg, which is about 20 times more [2].

For this reason, the development of a method capable of producing oxygen from water seems essential. **Figure 1.1** shows the electrolyzer, which helps to improve the efficiency of the water splitting process. An electrolyzer consists of a cathode, an anode,

and aqueous electrolyte. Hydrogen evolution reaction (HER) and oxygen evolution reaction (OER) takes place on the cathode and anode, respectively. The water splitting process is highly dependent on pH; thus different reactions are shown on the following equations [1]:

Acidic solution

(1) Cathode $2H^+ + 2e^- \rightarrow H_2$

(2) Anode $H_2O \rightarrow 2H^+ + 2e^- + \frac{1}{2}O_2$

In neutral and alkaline solutions

(1) Cathode $2H_2O + 2e^- \rightarrow H_2 + 2OH^-$

(2) Anode $2OH^- \rightarrow H_2O + 2e^- + \frac{1}{2}O_2$

Total reaction $H_2O \rightarrow H_2 + \frac{1}{2}O_2$

It is worth noting that transfer of four electrons is required to produce oxygen gas and OER involves multiple step reactions, which results in sluggish OER kinetics [3]. Based on thermodynamic consideration, the water splitting voltage is 1.23 V at 25 °C regardless of media. However, in reality, extra voltage, called “overpotential” should be applied for water splitting. Therefore, efficient electrocatalysts are needed to reduce the overpotential for the breakdown of water.

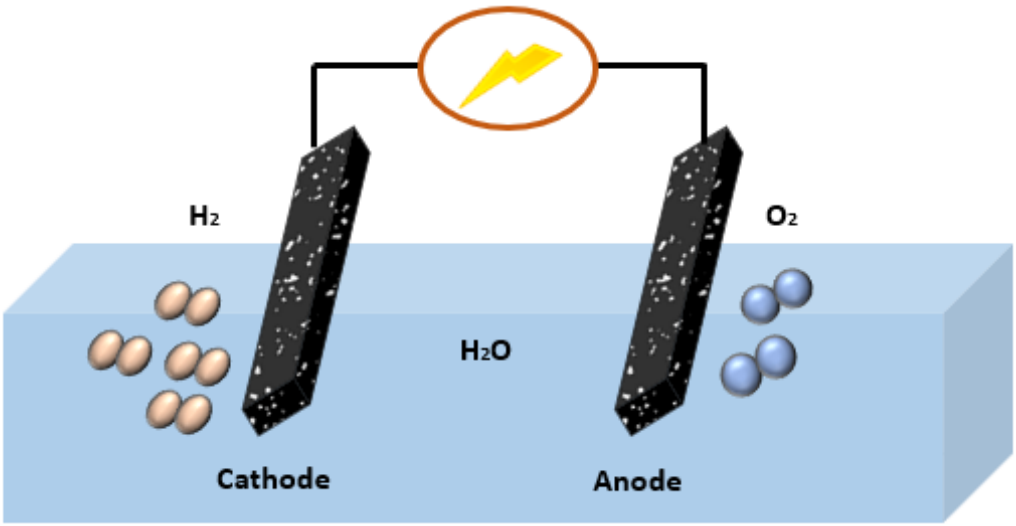

Figure 1.1: Schematic illustration of the electrolyzer.

Noble materials are considered the most effective materials for electrocatalysts. For example, platinum (Pt) displays excellent activity towards HER, while iridium (Ir) and ruthenium (Ru) show highly efficient performances towards OER [4]. However, since the above-mentioned materials are rare and expensive, various efforts are being made to discover or develop materials that are as abundant and inexpensive as possible while providing performance as good as noble materials. An example of the typical material is a transition metal oxide because transition metal oxide-based electrode materials are earth-abundant and show high electrochemical activity and stable performance [5].

Although the performance of transition metal oxide is good, it still needs further development compared to noble materials. Therefore, there are many efforts to improve the electrocatalytic properties and stability of transition metal oxide by using various strategies, such as material dimension reduction, composite formation, doping and functionalization, and morphology control, etc. For example, the He group synthesized mesoporous NiO/MnO_2 using inverse micelle templated UCT (University of

Connecticut) methods [6]. The material was utilized as an electrocatalyst material for oxygen evolution reaction and showed a low overpotential of 390 mV at 10 mA/cm^2. However, in order to improve the electrocatalytic activity of the material, the group coated PANI onto the surface of the NiO/MnO. It showed an improved conductivity of NiO/MnO_2@PANI material, which resulted in a lower overpotential of 345 mV.

1.3 Introduction of supercapacitor

A growing interest in electric vehicles (EVs) is driving demand for lithium-ion batteries. Because the specific energy of the lithium-ion battery is high, it is also widely used in various applications such as laptops and mobile phones. The layered $LiMO_2$ (M=Co, Ni, Mn) materials and graphite are most widely used as the cathode and anode materials for rechargeable Li-ion batteries [7]. A charge can be stored when the guest ion (Li ion) is inserted between each layer of the host materials. However, the ion diffusion within the bulk of crystalline materials restricts the charge/discharge rate of the battery, which results in poor power density [8]. For this reason, EVs using batteries have a big disadvantage, which is that the charging rate is too slow.

Unlike Li-ion batteries, supercapacitors are a promising energy storage device with fast charging and long cycle life [9]. This is because the charge storage mechanism of a supercapacitor is not diffusion of electrolyte in a layer structure material like a battery, but rather is a surface reaction of the electrode material. The energy storage capability of supercapacitor devices is higher than conventional capacitors, and their power delivery capability is higher than secondary batteries [10].

There are three main types of supercapacitors: (1) electric double-layer capacitors

(EDLCs), (2) pseudocapacitors, and (3) hybrid supercapacitors. These devices can be classified by the energy storage mechanism. First, EDLCs store the charge based on the adsorption of electrolyte on the surface of the material. **Figure 1.2** displays the schematic of electric double-layer structure [11].

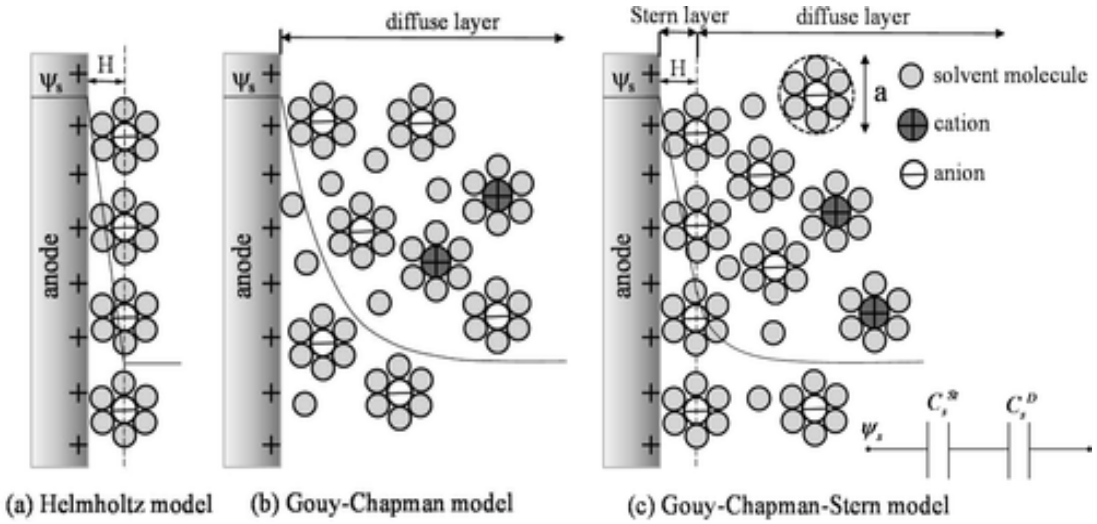

Figure 1.2: Electric double layer schematic of (a) Helmholtz model, (b) Gouy-Chapman model, and (c) Gouy-Chapman-Stern model. "Reproduced with permission from [11]. Copyright (2011) American Chemistry Society".

The electric double layer structure was first considered by Helmholtz. He suggested that electrical charge can be accumulated as solvated ions lined up along the surface of the electrode as shown in **Figure 1.2 (a)**. However, given the disordering effect of solvated ions, many ions would diffuse towards electrolyte [12]. Thus, **Figure 1.2 (b)** exhibited the concept of a diffusion layer introduced by Gouy and Chapman. Subsequently, Stern proposed the Gouy-Chapman-Stern model by combining the concepts of Helmholtz and Gouy-Chapman model, which became the most well-known

concept, the EDLC. Carbon-based materials are excellent candidates as the source of EDLCs due to their various properties, such as large surface area, high conductivity, and abundance. Consequently, several carbon materials (i.e., carbon nanotubes, activated carbons, and graphene) are widely investigated as the active materials for EDLCs [13].

Second, a pseudocapacitor predominately stores the energy via surface faradic redox reaction. The prefix of “pseudo” indicates the meaning of “false” or “fake”. As the prefix implies, a pseudocapacitor exhibits a different behavior from the conventional capacitor [14]. The characteristic of the device represents some point between EDLC and battery. The occurrence of faradic reaction deviates from the capacitor and enables pseudocapacitor to provide higher specific energy than EDLCs. The most commonly used materials for pseudocapacitors are transition metal oxide and conducting polymers, including ruthenium oxide (RuO_2), manganese dioxide (MnO_2), nickel oxide (NiO), cobalt oxide (Co_3O_4), polyaniline (PANI), polypyrrole (PPy), and poly (3,4-ethylenedioxythiophene) (PEDOT) [15].

Finally, hybrid supercapacitors are devices that combine the advantages of an EDLC and a pseudocapacitor into one device. Two types of hybrid supercapacitors are extensively studied: asymmetric hybrids and composite hybrids [16]. Asymmetric hybrids configure an EDLC type electrode (carbon-based materials) and pseudocapacitor type electrode (transition metal oxide or conducting polymer) as anode and cathode electrode, respectively. **Figure 1.3 (a)** shows a hybrid supercapacitor consisting of 3D graphene hydrogel and MnO_2@Ni foam as negative and positive electrodes, respectively [17]. The device showed stable operation in a wide potential window ranging from 0-2 V, a high maximum energy density of 23.2 Wh/kg and power

density of higher than 10 kW/kg, and stable 83.4% capacitance retention up to 5,000 cycles.

Unlike asymmetric hybrids, composite hybrids incorporate pseudocapacitor-based materials and EDLC-based materials into a single material. The combination of EDLC materials, with large surface area and high conductivity, and pseudocapacitor materials, with high specific capacitance derived from faradic reactions, can ensure improved energy storage properties. For example, **Figure 1.3 (b)** shows a MoS_2/PPy/rGO composite [18]. By integrating MoS_2 materials with PPy and rGO, the conductivity of the MoS_2 was improved and high specific capacitance of 1,942 F/g was achieved at the current density of 1 A/g.

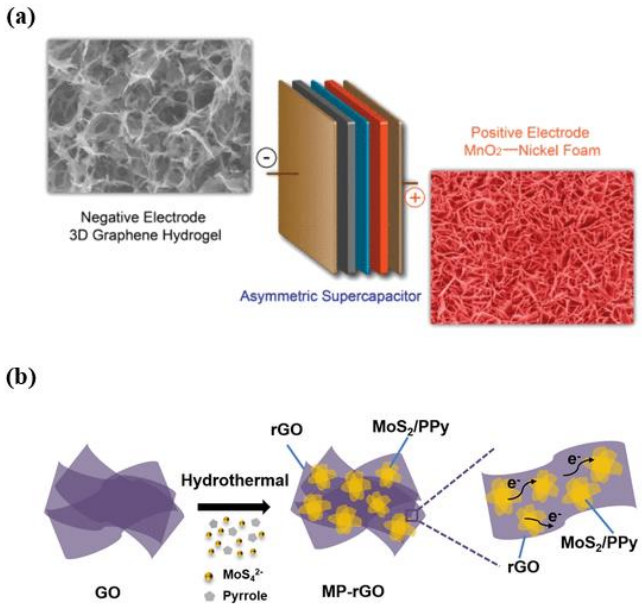

Figure 1.3: Hybrid supercapacitor: (a) asymmetric supercapacitor consisting of 3D graphene hydrogel and MnO_2@Ni electrodes. "Reproduced with permission from [17]. Copyright (2012) American Chemistry Society" and (b) rGO/MoS_2/PPy composite electrode materials. "Reproduced with permission from [18]. Copyright (2021) American Chemistry Society".

1.4 The objective of the thesis

Transition metal oxide-based materials are widely utilized as bifunctional materials in energy conversion and storage devices due to their rich active sites and easily tunable properties. However, the performance of transition metal oxides is still low compared to state-of-the-art materials. Therefore, the purpose of this study was to elevate the performance and stability of transition metal oxide for energy conversion and storage. First, for developing of the material, two different transition metal oxides were combined to produce a binary transition metal oxide (BTMO). Then, in order to improve the conductivity of the material, rGO and PANI were combined with several BTMOs to make a ternary composite material. For detailed analysis of the ternary composite materials, various structure and electrochemical characterizations were carried out.

CHAPTER II

EXPERIMENTAL DETAILS

2.1. Materials

Nickel (II) acetate {$Ni(CH_3CO_2)_2$} tetrahydrate, cobalt (II) acetate {$Co(CH_3CO_2)_2$} tetrahydrates, manganese (II) acetate {$Mn(CH_3CO_2)_2$} tetrahydrates, ammonium oxalate {$(NH_4)_2C_2O_4$}, potassium persulfate {$K_2S_2O_8$}, graphene oxide (GO), and aniline were purchased from Fisher Scientific, USA. Also, polyvinylidene fluoride (PVDF), N-methyl-2- pyrrolidone (NMP), carbon black, and KOH pellets were purchased from MTI Corporation, USA.

2.1.1 Binary transition metal oxide

Various transition metal oxides (i.e., NiO, Co_3O_4, Fe_2O_3, and MnO_2) have been widely utilized as materials for energy conversion and storage devices due to several advantages, such as abundant active sites and high redox activity [19]. Therefore, many modifications of the structure and morphology of transition metal-based materials have been conducted to enhance the performance. Recently, the construction of BTMOs (i.e., $ZnFe_2O_4$, $NiCo_2O_4$, $CoFe_2O_4$, $NiFe_2O_4$, and $MnFe_2O_4$) has emerged as a promising way to enhance the electrochemical properties [19]. BTMOs exhibit the synergy effect by combining the properties of each metal oxide.

Based on findings of several studies, the combination of each TMO not only reduced the volume expansion of TMOs, but also improved the electrical conductivity [20,21]. For example, the Tarasevich group found that the conductivity of $NiCo_2O_4$ is more than twice that of NiO and Co_3O_4, respectively [22]. Consequently, attention to BTMOs has increased rapidly. For example, $NiCo_2O_4$, $NiMn_2O_4$ $CoMn_2O_4$ are extensively studied due to their high electrochemical performance, low cost, easily tunable properties, and lower toxicity [23–28]. Therefore, these materials have been extensively employed in various applications, such as sensors, supercapacitors, batteries, and electrocatalysts [29–31].

2.1.2 Reduced graphene oxide

Graphene oxide and reduced graphene oxide possess large surface area, excellent electrical and thermal conductivity, outstanding chemical stability, and good mechanical strength [32]. GO is the family group of graphene. It can be easily produced by the reaction between graphite and an oxidizing agent. GO has various oxygen functional groups, such as carboxyl (C=O), epoxy groups (C-O), and hydroxyl (C-OH) [33]. Depending on the synthesis methods and conditions, the position and distribution of functional groups can vary, resulting in different material properties. rGO is a form of GO. It can be synthesized by the reduction of graphene oxide via several reduction processes i.e., hydrothermal, chemical reduction, and photo catalytic processes [34]. During the reduction process, oxygen-containing functional groups are removed. **Figure 2.1** exhibits the production process of GO and rGO from graphite.

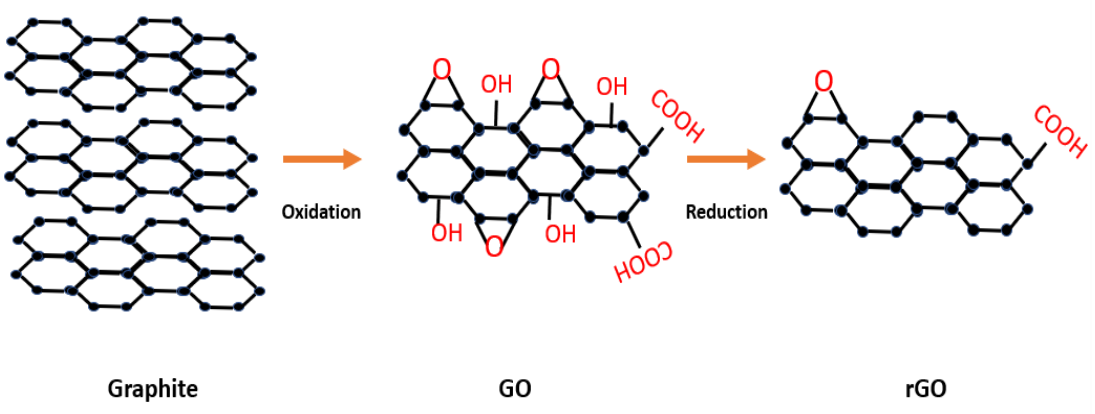

Figure 2.1: Schematic illustration of the graphite, GO, and rGO.

2.1.3 Polyaniline

Polyaniline is a conducting polymeric material. It can be easily produced by aniline oxidation via chemical or electrochemical process. PANI displays favorable properties of high conductivity, environmental thermal stability, and low cost, which make it an effective material for energy applications [35]. Chemical structure of PANI is shown in **Figure 2.2**. PANI is effectively utilized as a conducting agent or active materials for pseudocapacitor electrodes due to its multiple oxidation states [36]. However, based on some research, swelling and shrinkage of the polyaniline was observed during the redox reaction [37]. Moreover, performance degradation was noticed at high potential due to the generation of over-oxidation. Thus, these phenomena led to the low cycling stability of the polymeric material and prevented the extensive usage of the material for supercapacitor electrodes.

As a result, much research has been conducted to solve the issue of the material, and it was discovered that producing composite materials is an effective method to improve the mechanical stability, chain structure, and electrochemical performances [38]. PANI materials are usually integrated with carbon-based materials or metal oxide

materials to produce composite materials, which exhibit the enhanced property of the composite materials due to the synergy effect of each material [39,40].

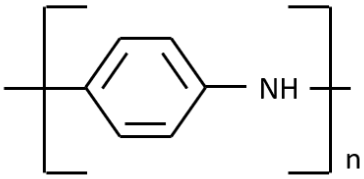

Figure 2.2: The chemical structure of polyaniline.

2.2. Synthesis of binary/ternary composite materials

2.2.1 Synthesis of $NiCo_2O_4$, $NiMn_2O_4$, $MnCo_2O_4$

$NiCo_2O_4$ was synthesized by the facile hydrothermal technique. First, $Ni(CH_3COO)_2$ solution (5 ml of 0.1 mol/l) and $Co(CH_3COO)_2$ (10 ml of 0.1 mol/l) were mixed, then stirred for 30 min at room temperature. After that, $(NH_4)_2C_2O_4$ solution (20 ml of 0.1 mol/l) was added to the mixture solution and stirred for 2 h. The mixture was transferred to a 45 ml capacity Teflon-lined stainless-steel vessel and heated 180 °C for 6 h. When the reactor cooled to room temperature, the product was collected by centrifuge and washed with DI water and ethanol. The powder was dried at 60 °C for 12 h, then it was annealed at 450 °C for 1 h.

For the preparation of $NiMn_2O_4$, $Ni(CH_3COO)_2$ solution (5 ml of 0.1 mol/l) and $Mn(CH_3COO)_2$ (10 ml of 0.1 mol/l) were utilized. In $MnCo_2O_4$, $Mn(CH_3COO)_2$ solution (5 ml of 0.1 mol/l) and $Co(CH_3COO)_2$ (10 ml of 0.1 mol/l) were combined. The synthesis of $NiMn_2O_4$ and $MnCo_2O_4$ materials further followed the same procedure as for the synthesis of $NiCo_2O_4$.

2.2.2 Synthesis of rGO/$NiCo_2O_4$, rGO/$NiMn_2O_4$, rGO/$MnCo_2O_4$

First, GO (60 mg) was dispersed in DI water (12 ml). Then, $Ni(CH_3COO)_2$ (3 ml of 0.1 mol/l) and $Co(CH_3COO)_2$ solution (6 ml of 0.1 mol/l) were added to the GO dispersion, and stirred at room temperature for 30 min. After that, $NH_4C_2O_4$ solution (12 ml of 0.1 mol/l) was added to the GO containing solution and stirred using sonication for 2 h. The solutions were then transferred into the autoclave reactor and heated at 180 °C for 6 h. Once it reached the room temperature, the remaining powder was collected by filtration. The collected powder was dried at 60 °C for 8 h and annealed at 450 °C for 1 h to synthesize the rGO/$NiCo_2O_4$ material.

Likewise, rGO/$NiMn_2O_4$ material was prepared through the same process sequence as rGO/$NiCo_2O_4$ after using $Ni(CH_3COO)_2$ (3 ml of 0.1 mol/l) and $Mn(CH_3COO)_2$ (6 ml of 0.1 mol/l).

Also, $Mn(CH_3COO)_2$ (3 ml of 0.1 mol/l) and $Co(CH_3COO)_2$ solution (6 ml of 0.1 mol/l) were mixed for the synthesis of rGO/$MnCo_2O_4$.

2.2.3 Synthesis of rGO/$NiCo_2O_4$/PANI, rGO/$NiMn_2O_4$/PANI, rGO/$MnCo_2O_4$/PANI

In-situ polymerization process of aniline occurred in each binary composites for the synthesis of the ternary composite materials. In 1 M H_2SO_4 (100 ml), aniline (0.1 ml) was dispersed in an ice water bath. Once the suspension containing aniline was uniform, each binary composite (rGO/$NiCo_2O_4$, rGO/$NiMn_2O_4$, rGO/$MnCo_2O_4$) (100 mg) was added to the aniline solution and mixed for 30 min. In an ice water bath, $K_2S_2O_8$ (1 g) was slowly added to the solution and stirred for 3 h. The mixture was maintained at 0-5 °C for 12 h, and final products (rGO/$NiCo_2O_4$/PANI, rGO/$NiMn_2O_4$/PANI, rGO/$MnCo_2O_4$/PANI) were obtained after a process of filtering, cleaning, and drying.

Table 2.1: The sample name and codes of binary/ternary composite materials.

Sample Name	Sample Code	Sample Name	Sample Code
$NiCo_2O_4$	NCO	$rGO/MnCo_2O_4$	GMCO
$NiMn_2O_4$	NMO	$rGO/NiCo_2O_4$/PANI	GNCOP
$MnCo_2O_4$	MCO	$rGO/NiMn_2O_4$/PANI	GNMOP
$rGO/NiCo_2O_4$	GNCO	$rGO/MnCo_2O_4$/PANI	GMCOP
$rGO/NiMn_2O_4$	GNMO		

2.3 Structure characterization

The structure and morphology of synthesized binary transition metal oxides, binary/ternary composite materials were investigated by X-ray photo-electron spectroscopy (XPS) (Thermo Scientific K-alpha), X-ray diffraction (XRD) (Columbia, MD, USA), and scanning electron microscopy (SEM) (Phenom, Oak Park, CA, USA).

2.3.1. XPS

XPS was used to study the chemical states, the chemical composition, the atomic weight percentage, and binding energy of the as-prepared samples. The surface investigation of all materials was conducted using X-rays. First, an X-ray beam hit the material, then the X-ray induced the excited electrons from the inner shell electrons, which are called “photo-emitted electrons.” The detector probed the kinetic energy of photo-emitted electrons to generate the spectrum of all samples. All measurements were conducted under vacuum conditions, and XPS with Al Kα line (hv=1486.6 eV) was employed.

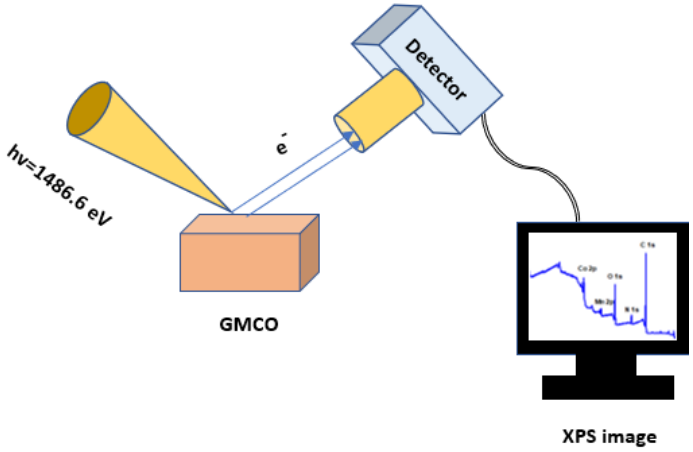

Figure 2.3: Schematic of XPS.

2.3.2. XRD

XRD measurement was utilized to study the structure and phase purity of all synthesized material. The XRD mainly consists of an X-ray tube and detector. The X-ray generated from the tube hit the sample in the middle of the instrument, then the scattered X-ray was recorded by the detector. As the X-ray tube synchronized with the detector, X-ray diffraction patterns were observed at different angles. The structure and phase of crystalline material was investigated based on Bragg's law ($2d \sin\theta = n\lambda$) where n is order of reflection, λ is the wavelength of X-rays, d is the inter-planner spacing, and θ is diffracted angle. The XRD pattern of all samples were obtained by Shimadzu X-ray diffractometer (XRD, CuKα1 λ = 1.5406 Å).

Figure 2.4: Images of Shimadzu X-ray diffractometer.

2.3.3. SEM

SEM was employed to investigate the morphology of all synthesized materials. The sample's morphology was obtained as electrons generated from electron beams bombaring the sample. The interaction between the incident electron and the sample can produce X-rays, Auger electrons, backscattered electrons, and secondary electrons. The SEM image is produced by detection of the secondary electrons (all images were acquired at 10 keV).

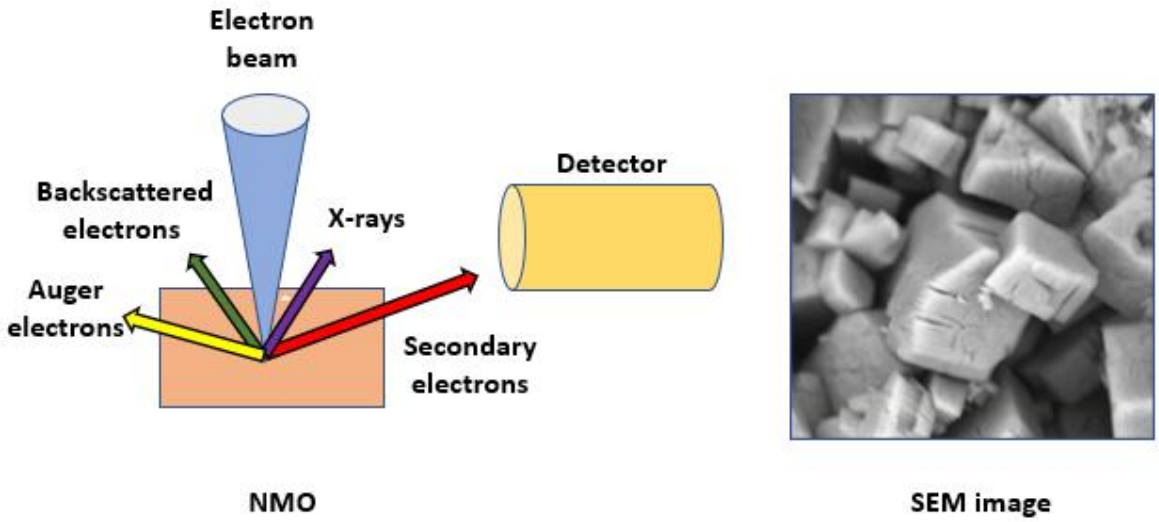

Figure 2.5: Schematic of SEM and SEM image of NMO.

2.4. Electrochemical characterization

Electrochemical characterization of all samples was studied using a PARSTAT MC electrochemical workstation (Princeton Applied Research, USA) in conventional three electrode systems. Three electrode systems consist of working, counter, and reference electrodes. First, a working electrode was prepared by mixing 80 wt% synthesized materials (active material), 10 wt% PVDF (binder), and 10 wt% carbon black (conductive additive) in the presence of NMP solvent. The Ni foam (substrate) was dipped into the paste and dried at 60 °C 48 h. Platinum wire (Pt) was used as a counter electrode, and saturated calomel electrode (SCE) or Hg/HgO was used as a reference electrode for the study of its performance in water splitting and its characteristics as a supercapacitor, respectively. For the study of its characteristics as an electrocatalyst, linear sweep voltammetry (LSV), chronoamperometry (CA), and electrochemical impedance spectroscopy (EIS) measurements were performed in 1 M KOH electrolyte.

In the case of supercapacitor testing, the cyclic voltammetry (CV) and galvanostatic charge-discharge (GCD) measurements were employed in 3 M KOH media for the analysis of energy storage properties.

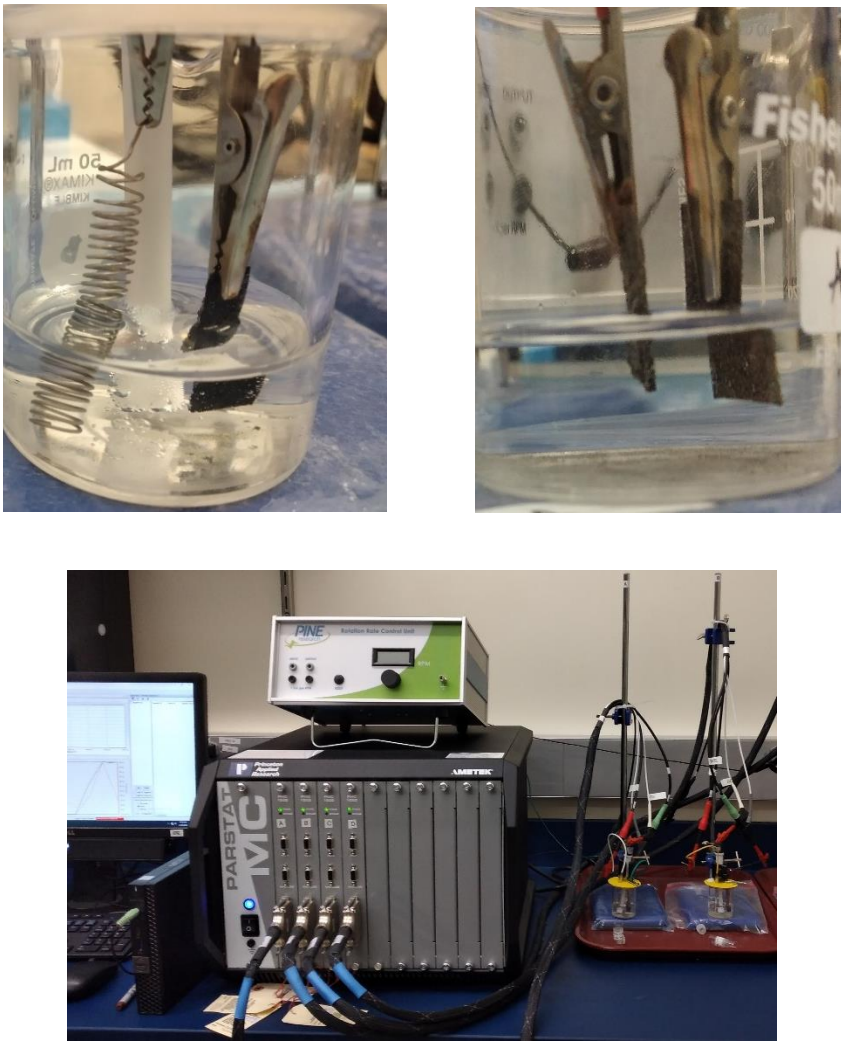

Figure 2.6: Images of 3 electrode configuration (top-left), 2 electrode configuration (top-right), PARSTAT MC electrochemical workstation (bottom).

CHAPTER III

RESULTS AND DISCUSSION

3.1 Structure characterization

3.1.1 XPS

XPS measurements were utilized to investigate the chemical composition of all materials. **Figure 3.1 (a-c)** shows the survey spectrum of NCO, GNCO, and GNCOP samples. All materials contain 4 elements of Ni, Co, O, and C. In addition, the presence of N element was observed from the GNCOP material due to the existence of polyaniline in composite material. To further identify the GNCOP material, the high resolution of the material was presented. **Figure 3.1 (d)** shows the Ni $2p_{1/2}$ spectrum with Ni^{2+} (871.6 eV) and Ni^{3+} (873.5 eV), the Ni $2p_{3/2}$ spectrum with Ni^{2+} (853.8 eV) and Ni^{3+} (855.8 eV), and two satellite peaks (861.3 and 879.9 eV) [41]. As seen in **Figure 3.1 (e)**, Co 2p XPS spectrum have the major Co^{3+} and Co^{2+} peaks at 794.6 and 796.3 eV for $2p_{1/2}$, as well as Co^{3+} and Co^{2+} peaks at 779.5 and 780.9 eV for $2p_{3/2}$ [42]. **Figure 3.1 (f)** shows the O 1s core level spectrum with the peak at 529.4 eV, which is due to the metal-oxygen bond. Also, the peak at 531.0 eV corresponds to the OH^- group. In addition, impurities and surface defects might affect the presence of peak at 533.4 eV. In **Figure 3.1 (g)**, three peaks were observed at the binding energy of 284.2, 285.4, 287.3 eV, which is related to carbon functional groups of C−C, C−N, and C=O,

respectively. Moreover, three peaks were observed at 399.5, 402, 405.7 eV in N 1s spectrum, which is attributed to the presence of -N=, -NH- functional groups, and the interaction between N^+ and protons [43].

Likewise, **Figure 3.2 (a-c)** and **Figure 3.3 (a-c)** shows the survey spectrum of NMO and MCO based materials. Four different elements of Ni, Mn, O, C and Mn, Co, O, C were detected by NMO and MCO-based materials, respectively. Similarly, the nitrogen existed for GNMOP and GMCOP composite materials. In **Figure 3.2 (e)**, the Mn 2p spectrum was investigated in detail at a high resolution. Two peaks of Mn $2p_{3/2}$ and Mn $2p_{1/2}$ configurations were observed at 641.6 and 653.4 eV, which was ascribed to the Mn^{3+} and Mn^{2+}, respectively [44]. The spectrum of other elements showed similar characteristics to those of NCO-based materials.

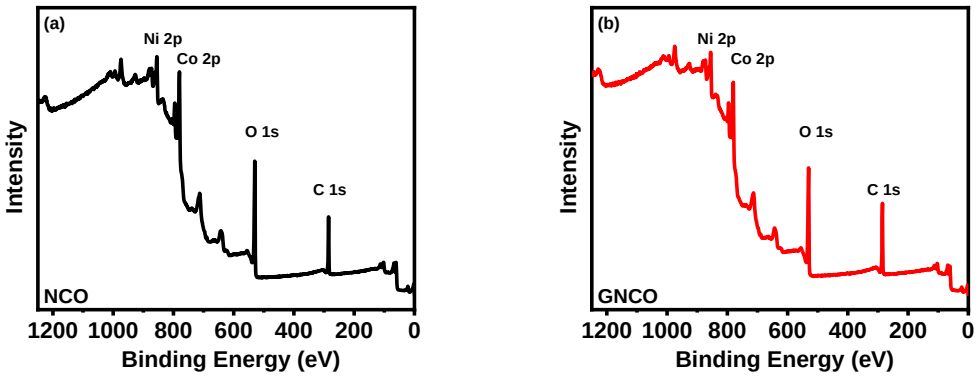

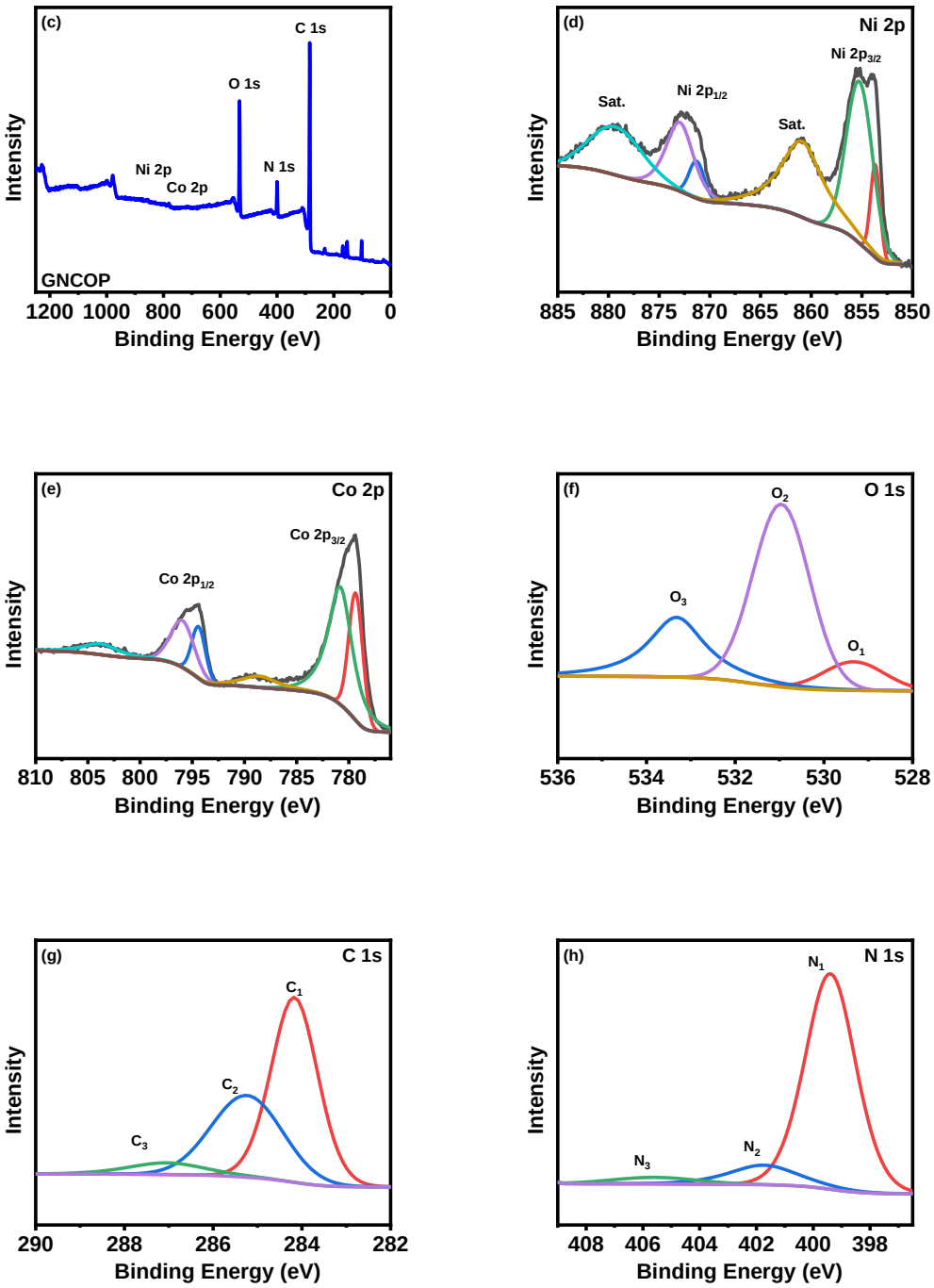

Figure 3.1: XPS survey spectra for (a) NCO, (b) GNCO, (c) GNCOP samples and high resolution of GNCOP for (d) Ni 2p, (e) Co 2p, (f) O 1s, (g) C 1s, and (h) N 1s.

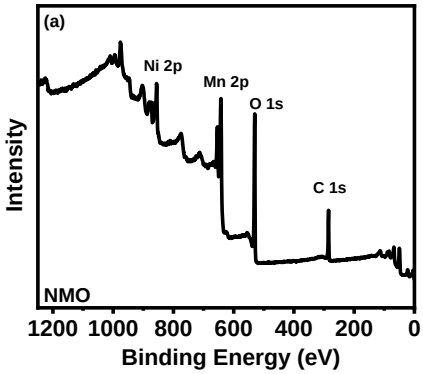
(a)
Ni 2p
Mn 2p
O 1s
C 1s
NMO
Intensity
1200 1000 800 600 400 200 0
Binding Energy (eV)

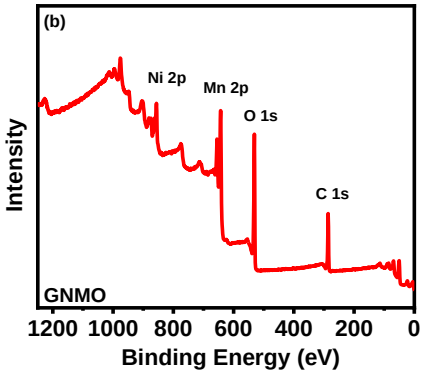
(b)
Ni 2p
Mn 2p
O 1s
C 1s
GNMO
Intensity
1200 1000 800 600 400 200 0
Binding Energy (eV)

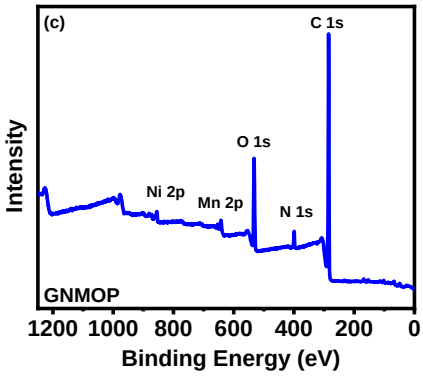
(c)
C 1s
O 1s
Ni 2p
Mn 2p
N 1s
GNMOP
Intensity
1200 1000 800 600 400 200 0
Binding Energy (eV)

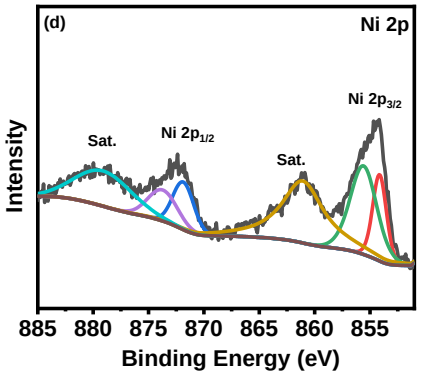
(d)
Ni 2p
Ni 2p3/2
Sat.
Ni 2p1/2
Sat.
Intensity
885 880 875 870 865 860 855
Binding Energy (eV)

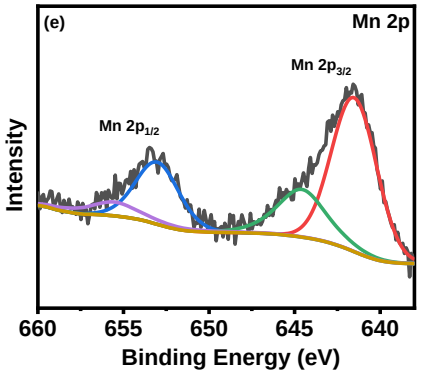
(e)
Mn 2p
Mn 2p3/2
Mn 2p1/2
Intensity
660 655 650 645 640
Binding Energy (eV)

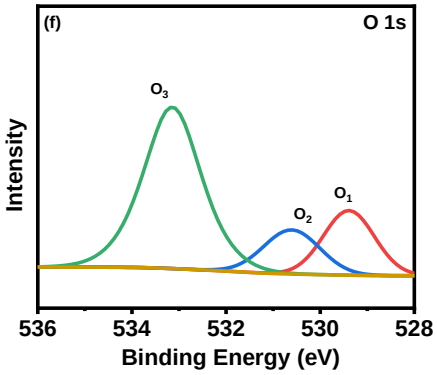
(f)
O 1s
O3
O2
O1
Intensity
536 534 532 530 528
Binding Energy (eV)

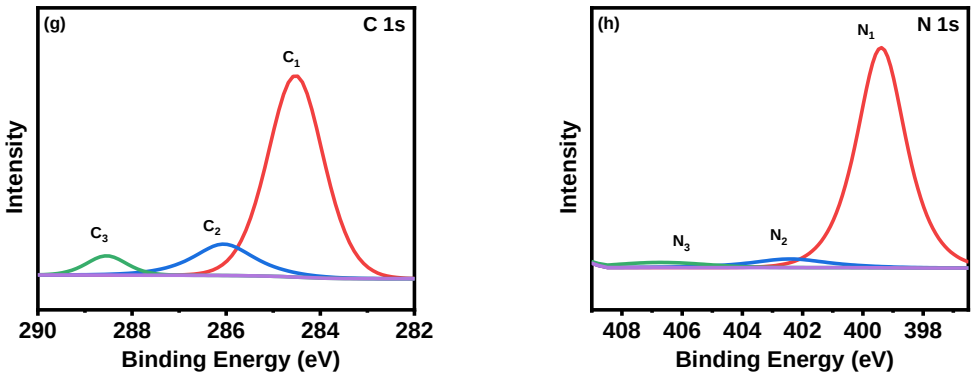

Figure 3.2: XPS survey spectra for (a) NMO, (b) GNMO, (c) GNMOP samples and high resolution of GNMOP for (d) Ni 2p, (e) Mn 2p, (f) O 1s, (g) C 1s, and (h) N 1s.

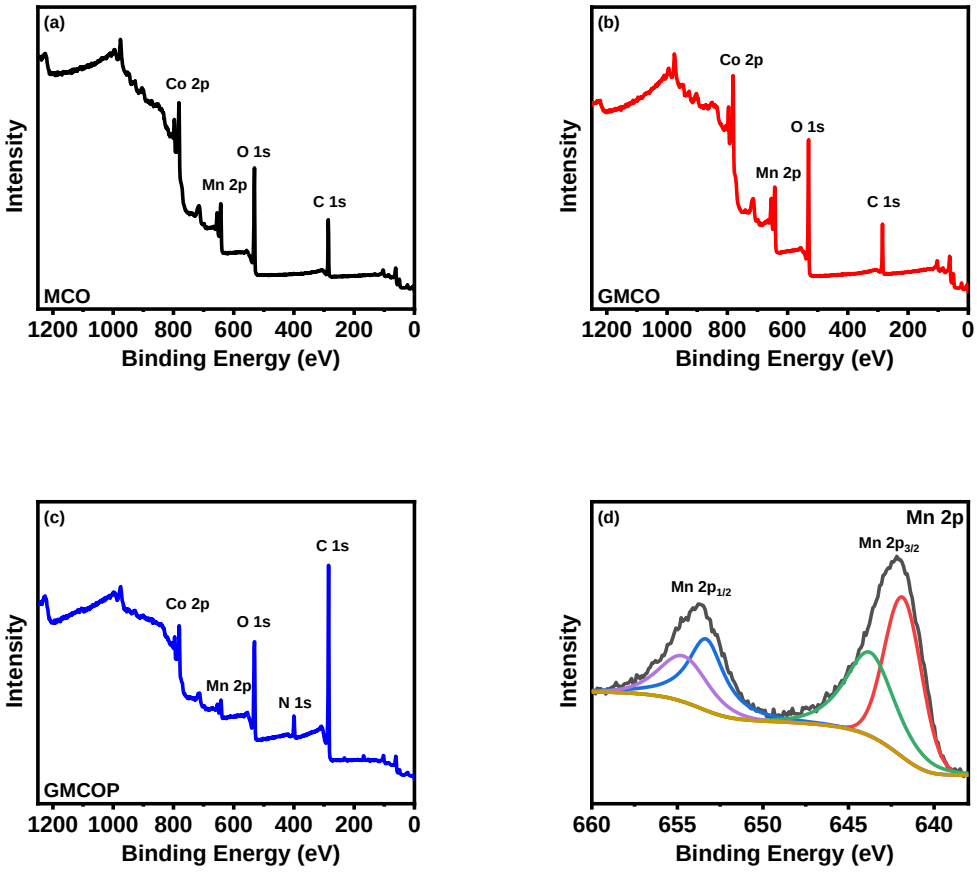

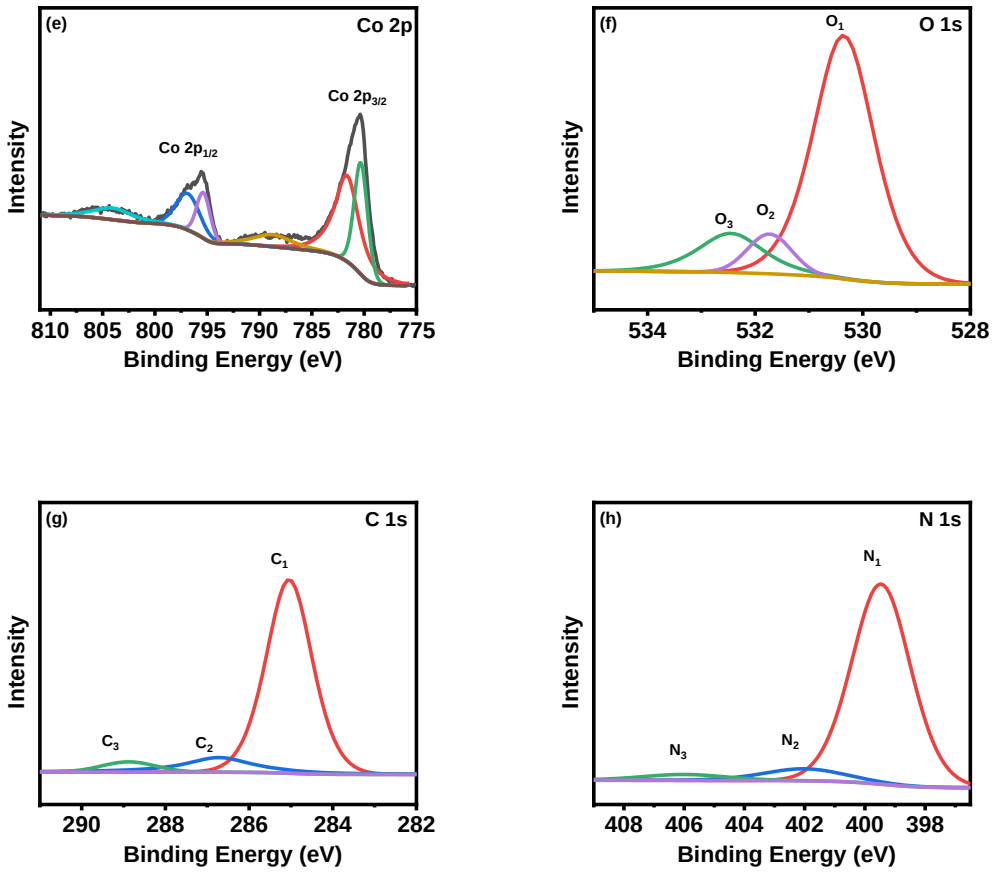

Figure 3.3: XPS survey spectra for (a) MCO, (b) GMCO, (c) GMCOP samples and high resolution of GMCOP for (d) Mn 2p, (e) Co 2p, (f) O 1s, (g) C 1s, and (h) N 1s.

3.1.2 XRD

XRD measurements of all materials were carried out in a range of 2θ = 10 to 80°. **Figure 3.4** shows the XRD spectrum of NCO-based materials. Peaks were observed at 30, 36, 45, 60, and 65°, which correspond to (220), (311), (400), (511), and (440) planes, respectively [45,46]. As seen in **Figure 3.5**, peaks of NMO based materials were located at 35 and 41°, which are indexed to (301) and (400) planes, respectively [47]. In addition, the peaks at 35, 42, 59, and 66° were shown in **Figure 3.6**, which is

attributed to the (311), (400), (511), and (531) planes, respectively [48]. These results indicates that each material has similar peaks of $NiCo_2O_4$, $NiMn_2O_4$, and $MnCo_2O_4$ materials, respectively. Most peaks were shown in the broader form, which is due to the poor crystallinity behavior of most materials.

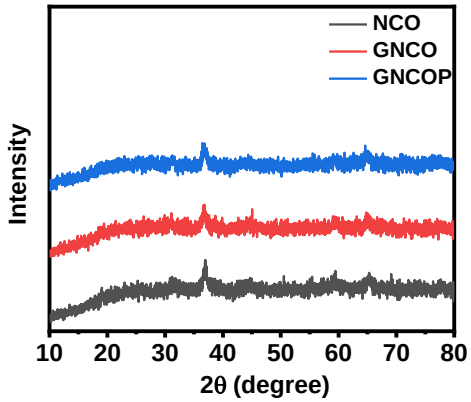

Figure 3.4: XRD pattern for NCO, GNCO, and GNCOP samples.

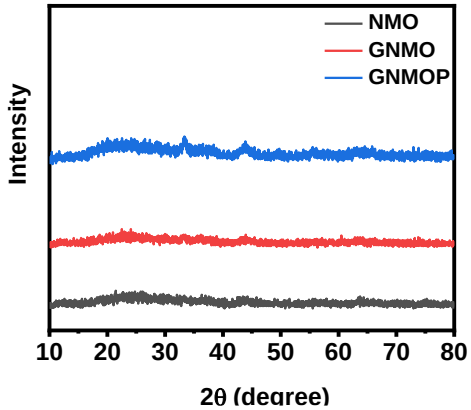

Figure 3.5: XRD pattern for NMO, GNMO, and GNMOP samples.

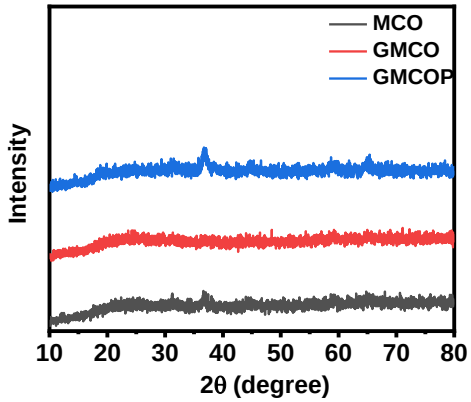

Figure 3.6: XRD pattern for MCO, GMCO, and GMCOP samples.

3.1.3 SEM

The morphology of all samples was studied using SEM measurements. As prepared samples were detected at high and low resolution. As seen in **Figure 3.7-9**, all materials possess rod-like structures, and the particles were well distributed. In addition, the reduction in particle size was observed when rGO and PANI were combined with binary transition metal oxide. The size reduction can help to enhance faster ion & electron transport and higher surface reactivity [49,50]. Consequently, a rod-like materials facilitates favorable electrochemical reaction for all samples, leading to excellent energy conversion and storage properties of all samples.

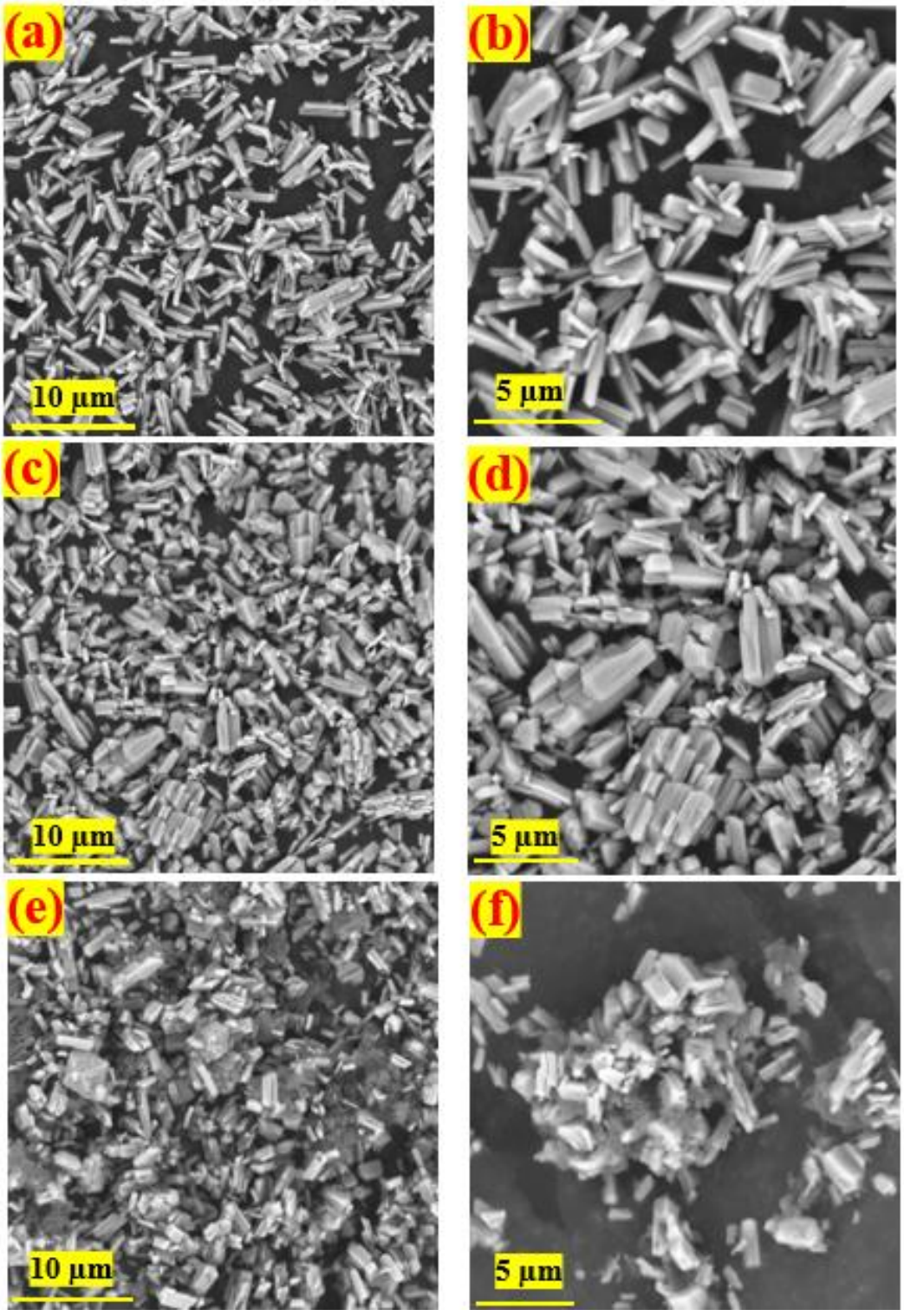

Figure 3.7: SEM images of (a,b) NCO, (c,d) GNCO, and (e,f) GNCOP materials at high and low resolutions.

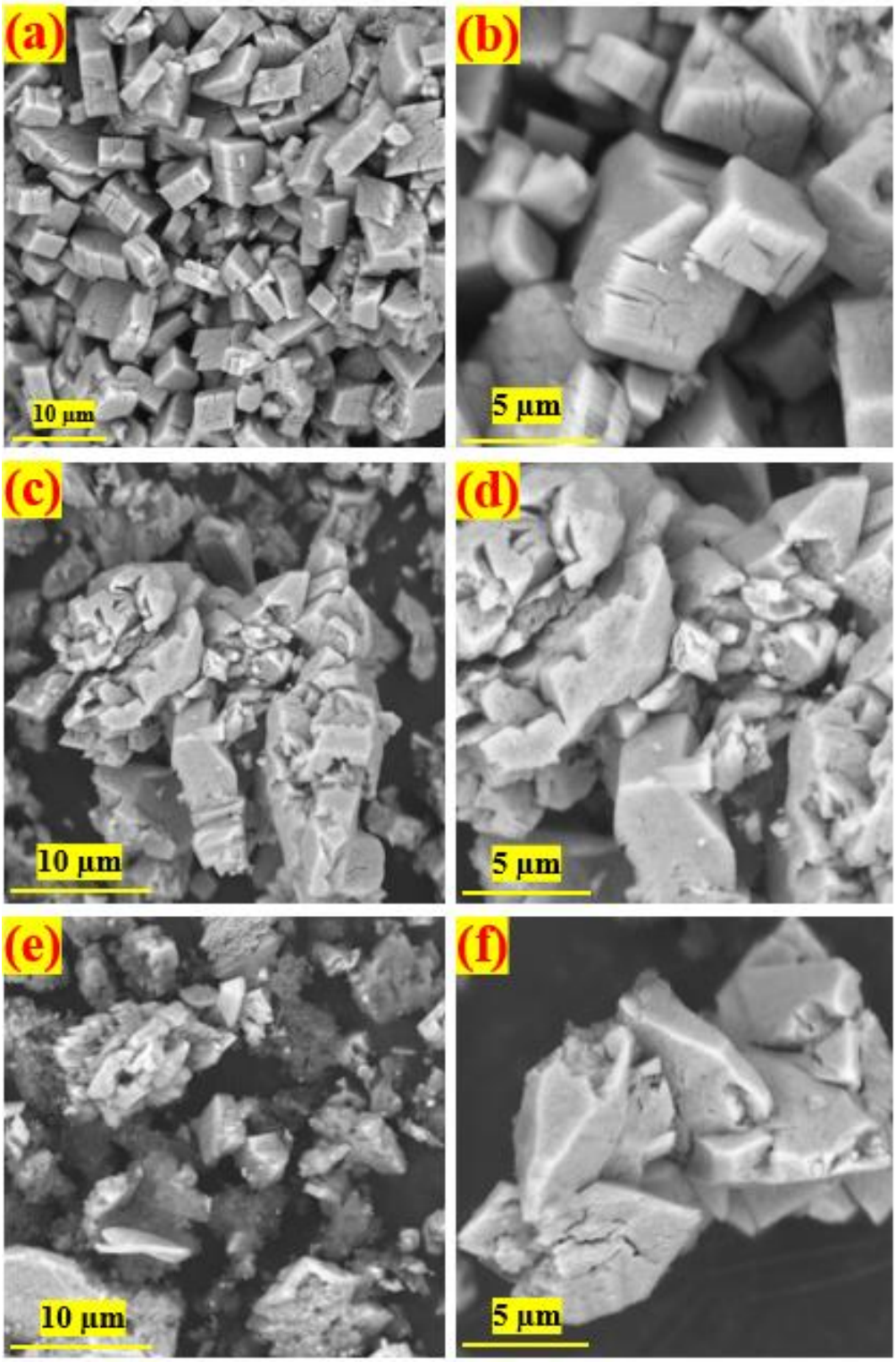

Figure 3.8: SEM images of (a,b) NMO, (c,d) GNMO, and (e,f) GNMOP materials at high and low resolutions.

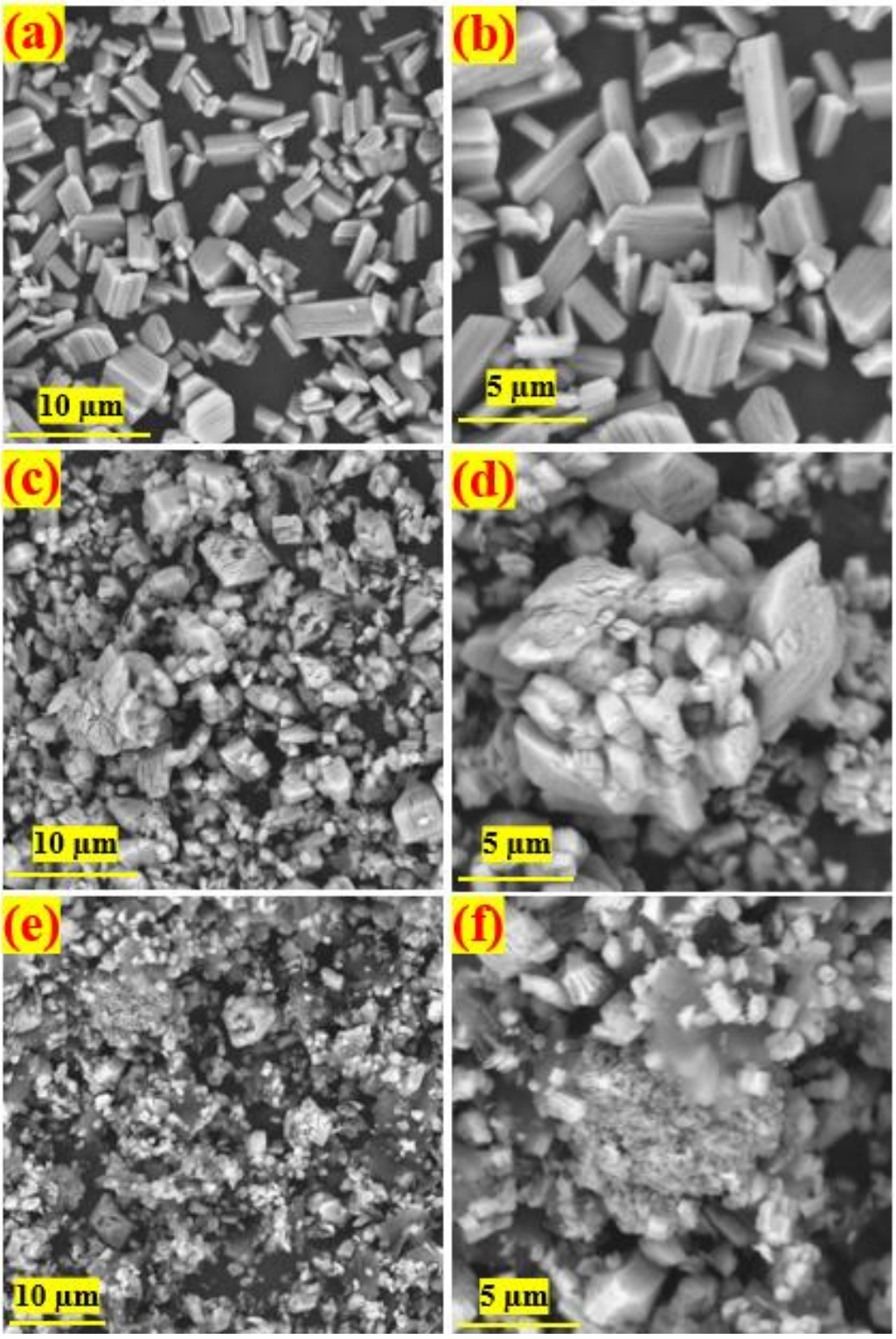

Figure 3.9: SEM images of (a,b) MCO, (c,d) GMCO, and (e,f) GMCOP materials at high and low resolutions.

3.2 Electrochemical measurements

3.2.1 Electrocatalytic performance towards water splitting

Figure 3.10 (a-c) shows the OER polarization curves of the as-prepared electrodes. These curves were obtained from the linear sweep voltammetry (LSV) measurements at a scan rate of 2 mV/s. The GNCOP, GNMOP, and GMCOP ternary composite-based electrodes showed a lower overpotential of 342, 340, and 382 mV respectively, while NCO, GNCO, NMO, GNMO, MCO, and GMCO electrodes required an overpotential of 350, 347, 421, 420, 388, and 385 mV respectively to reach the current density of 10 mA/cm^2. In addition, it was observed that most ternary composite-based electrodes generated higher current after the start of the reaction. For example, the current densities of 118, 78, and 44 mA/cm^2 for GNCOP, GNMOP, and GMCOP electrodes were achieved at a potential of 1.65 V, which is higher than other electrodes.

As shown in **Figure 3.11 (a-c)**, the Tafel slopes of all electrodes were plotted using the following equation (3.1) [51]:

$$\eta = a + b \log j \tag{3.1}$$

where η is the overpotential, a is the constant, b is Tafel slope, and j is the current density. Tafel slope of electrodes was 66, 58, 68, 104, 109, 83, 122, 75, and 65 mV/dec for NCO, GNCO, GNCOP, NMO, GNMO, GNMOP, MCO, GMCO, and GMCOP, respectively. A lower Tafel slope suggests faster kinetics of a material to produce oxygen gases [52].

In **Figure 3.12 (a-c)**, HER polarization curves of all electrodes were obtained at a scan rate of 2 mV/s. Overpotentials of 134, 95, and 117 mV were needed for GNCOP, GNMOP, and GMCOP electrodes respectively to produce the current density of 10

mA/cm^2. It shows that each ternary composite electrode had superior activity in comparison with each binary transition metal oxide and binary composite electrode i.e., NCO (168 mV), GNCO (161 mV), NMO (105 mV), GNMO (102 mV), MCO (128 mV), and GMCO (119 mV) electrodes. Also, most ternary composite GNCOP, GNMOP, and GMCOP electrodes generated higher current density of 115, 299, 222 mA/cm^2 at the potential of - 0.3 V (V, RHE) compared to other binary transition metal oxides and binary composite materials.

As seen in **Figure 3.13 (a-c)**, the Tafel slope of electrodes was calculated, which was 124, 144, 140, 154, 142, 135, 148, 130, and 123 mV/dec for NCO, GNCO, GNCOP, NMO, GNMO, GNMOP, MCO, GMCO, and GMCOP electrodes, respectively.

Figure 3.14 shows the Nyquist plots for all electrodes obtained by the EIS measurements at 1.65 V (V, RHE) in the range from 0.05 Hz to 10 kHz with an AC amplitude of 10 mV. **Figure 3.14 (a)** indicates the equivalent electrical circuit. R_1, R_2, and C suggests the electrolyte resistance, charge transfer resistance, and interfacial capacitance, respectively [53]. The starting point of the plot suggests electrolyte resistance. It displayed ~ 2.7 Ω for all electrodes since the experiment was conducted in the same alkaline media. Furthermore, the diameter of the semicircle representing the charge transfer resistance at the interface between electrode and electrolyte was 4.5, 3.1, 2.4, 17.3, 15.2, 7.4, 18.3, 6.8, 6.6 Ω for NCO, GNCO, GNCOP, NMO, GNMO, GNMOP, MCO, GMCO, and GMCOP, respectively. Given that the GNCOP, GNMOP, and GMCOP ternary composite-based electrodes have low overpotential, high current density at a given current density, low Tafel slopes, and low charge transfer resistance, these electrodes have superior electrocatalytic activity to split the water into hydrogen and oxygen gases.

The stability of the electrocatalysts is also one of the important factors to determine the effective electrocatalyst. To study the stability of all electrocatalysts, the comparison of LSV 1 vs LSV 1k curves and chronoamperometry measurement were employed. First, the LSV 1k graph was achieved by performing 1,000 CV cycles at the potential range of 0.2 – 0.55 V (V, SCE). As seen in **Figure 3.15** and **Figure 3.16**, only slight differences between the graphs were observed from all samples. Besides, stable i-t curves were observed measured by CA experiment at the high potential of 1.6 V (V, RHE) for a long period of time, as shown in **Figure 3.17**. All electrodes showed stable performance even at high current density, and the slight fluctuations observed in the graph are due to gas generation.

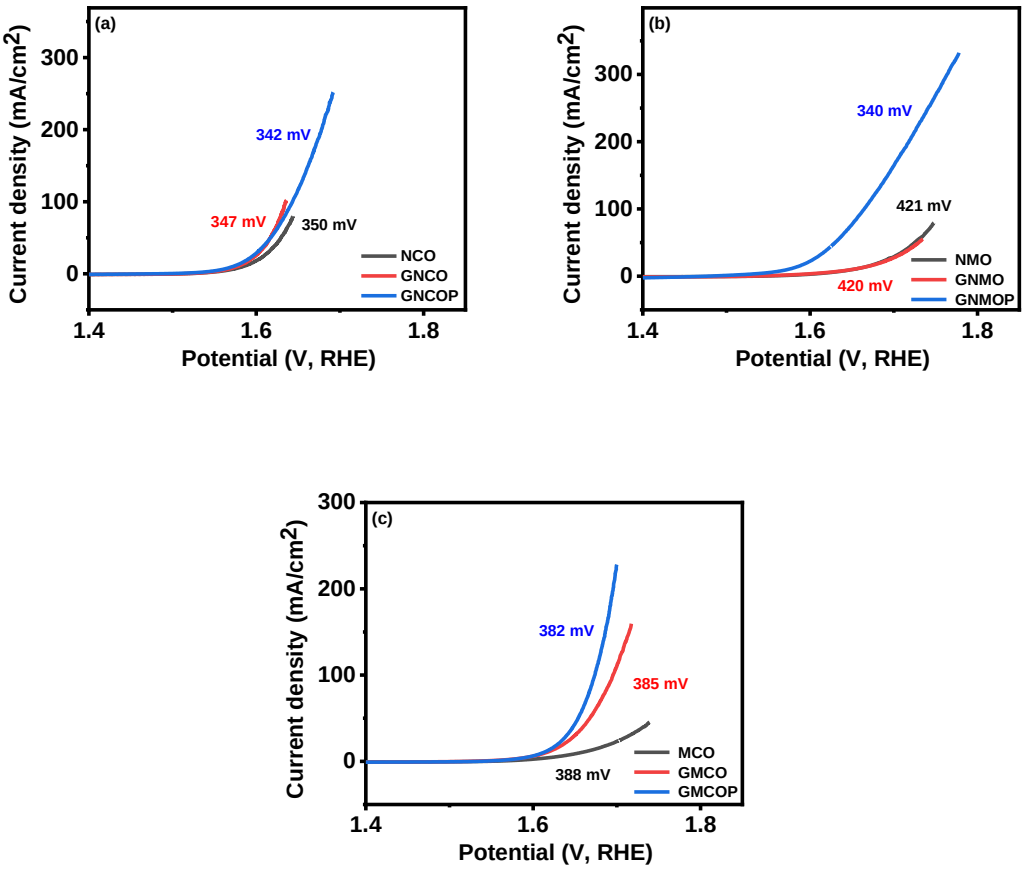

Figure 3.10: OER polarization curves of all electrodes.

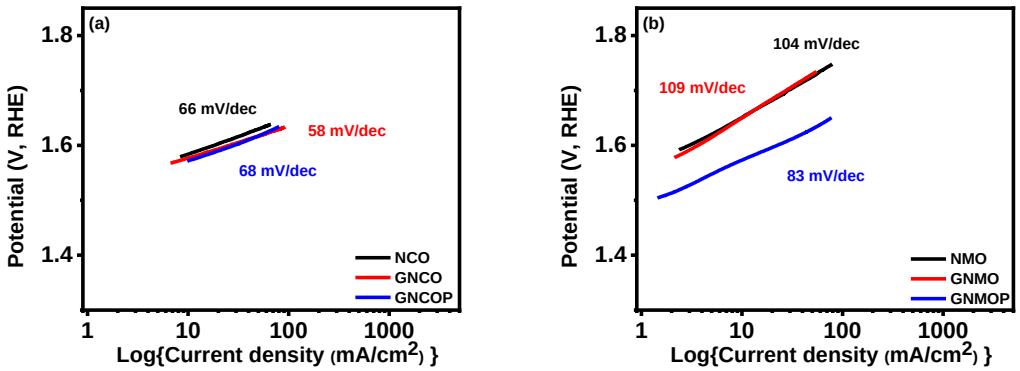

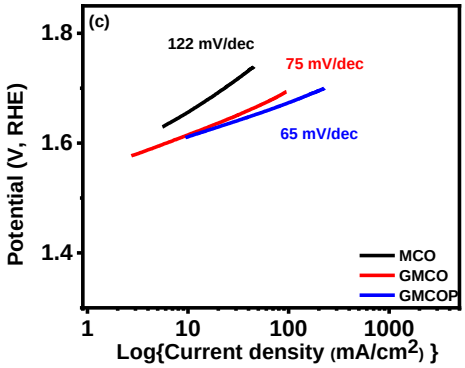

Figure 3.11: Tafel slopes of all electrodes for the OER.

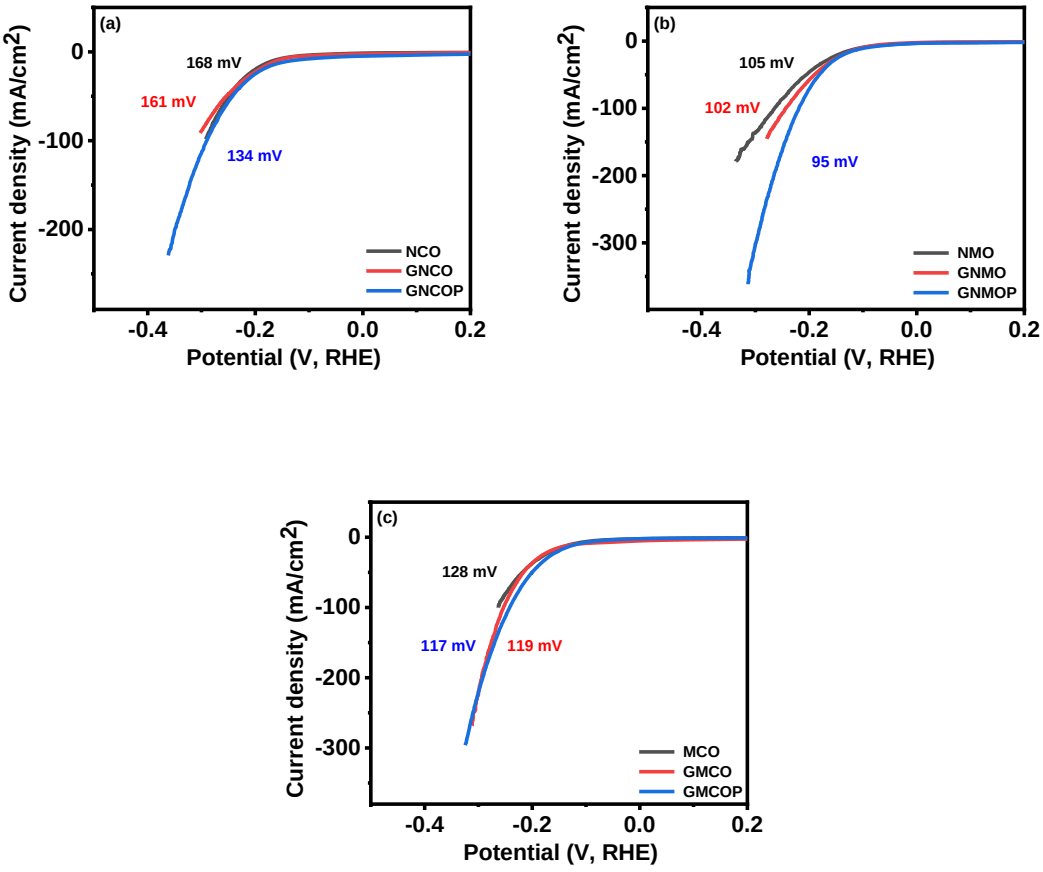

Figure 3.12: HER polarization curves of all electrodes.

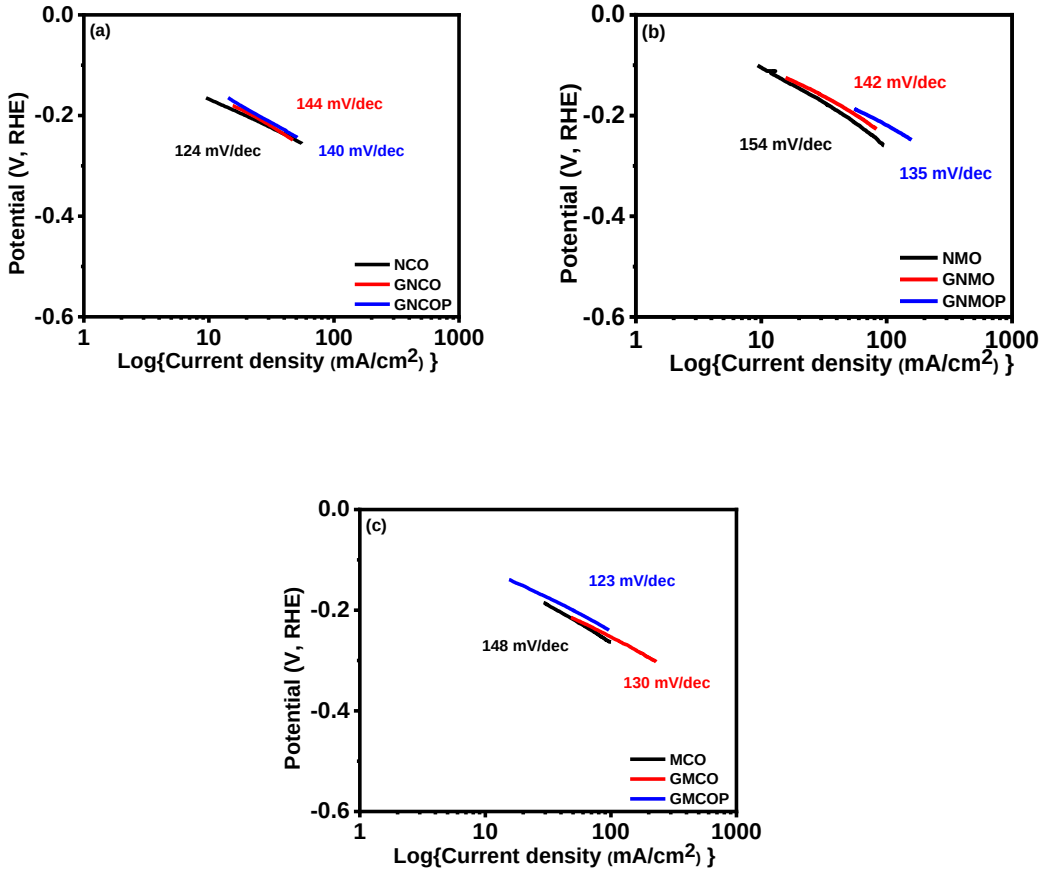

Figure 3.13: Tafel slopes of all electrodes for the HER.

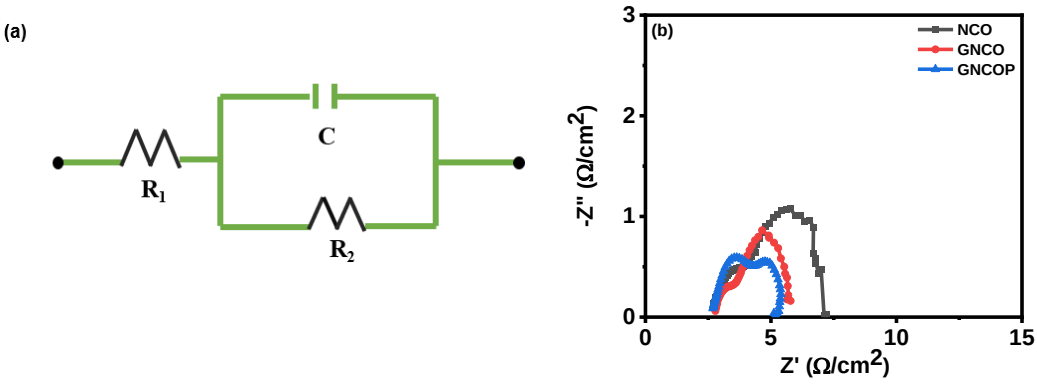

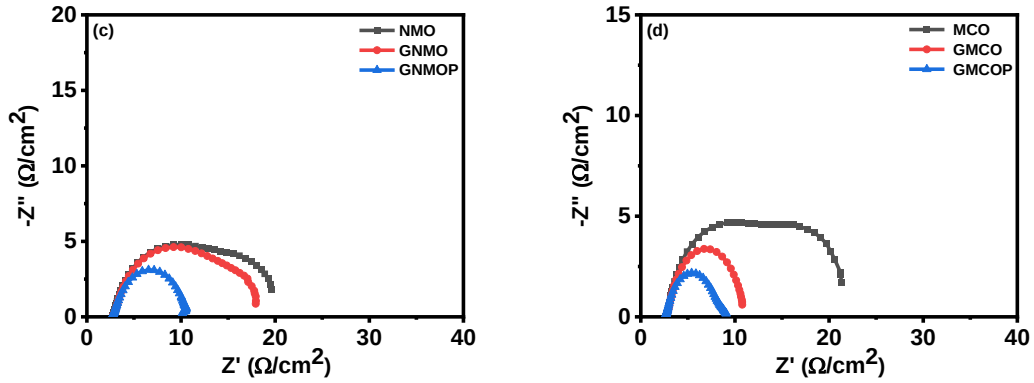

Figure 3.14: (a) Schematic of an electrical circuit, (b-d) the Nyquist plot of all electrodes at 1.65 V (V, RHE).

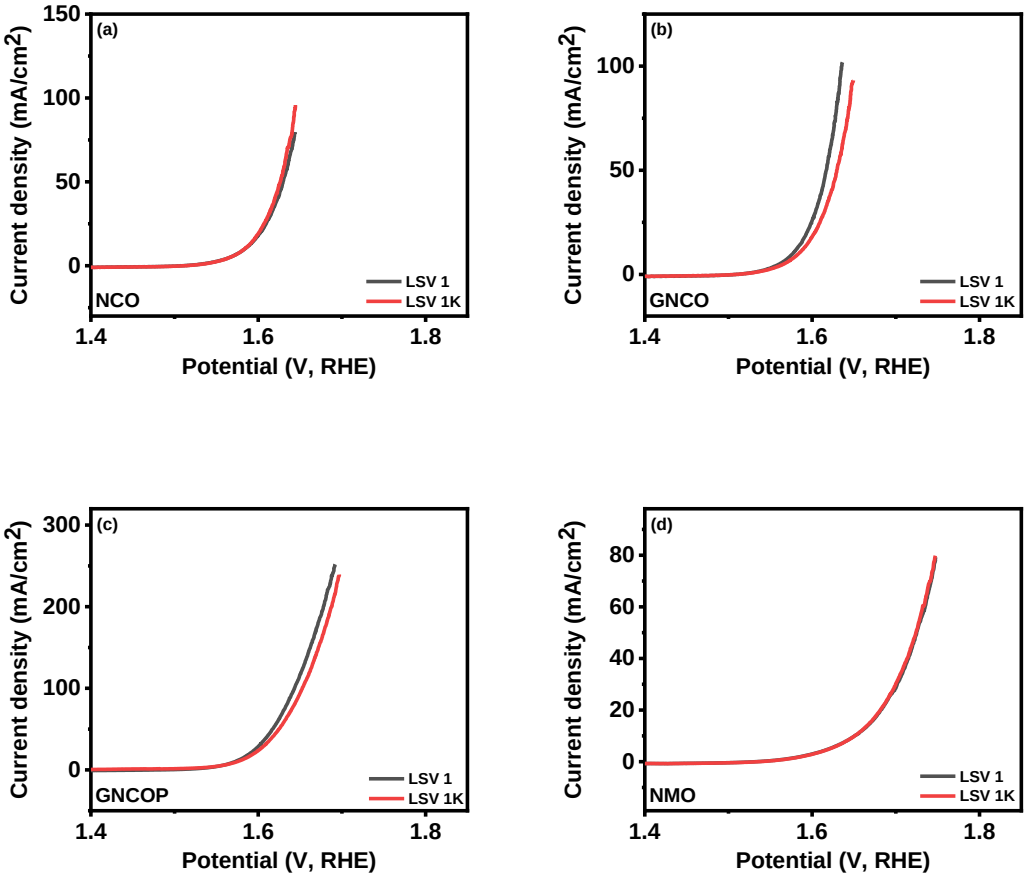

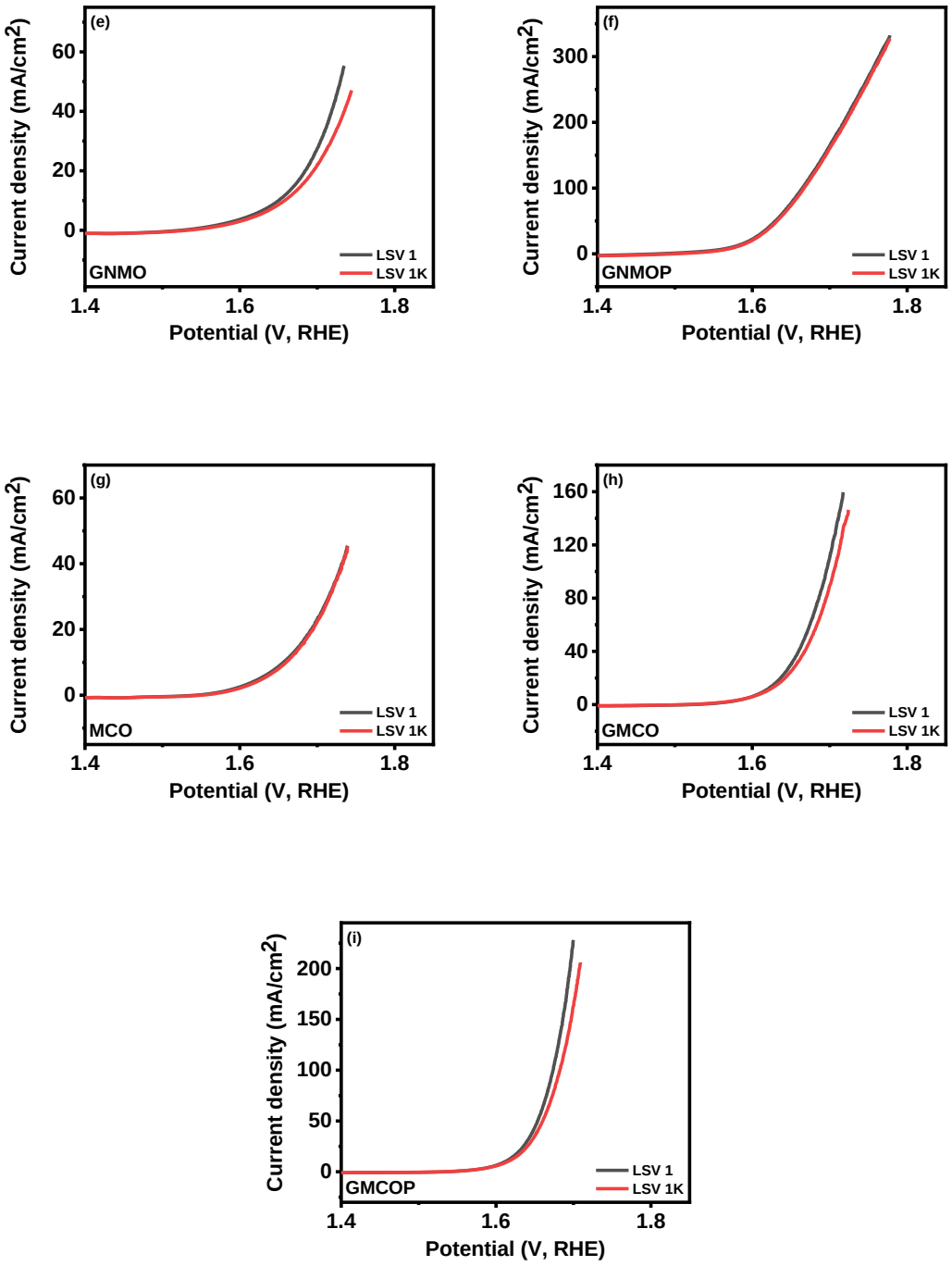

Figure 3.15: 1 vs 1k OER polarization curves of all electrodes.

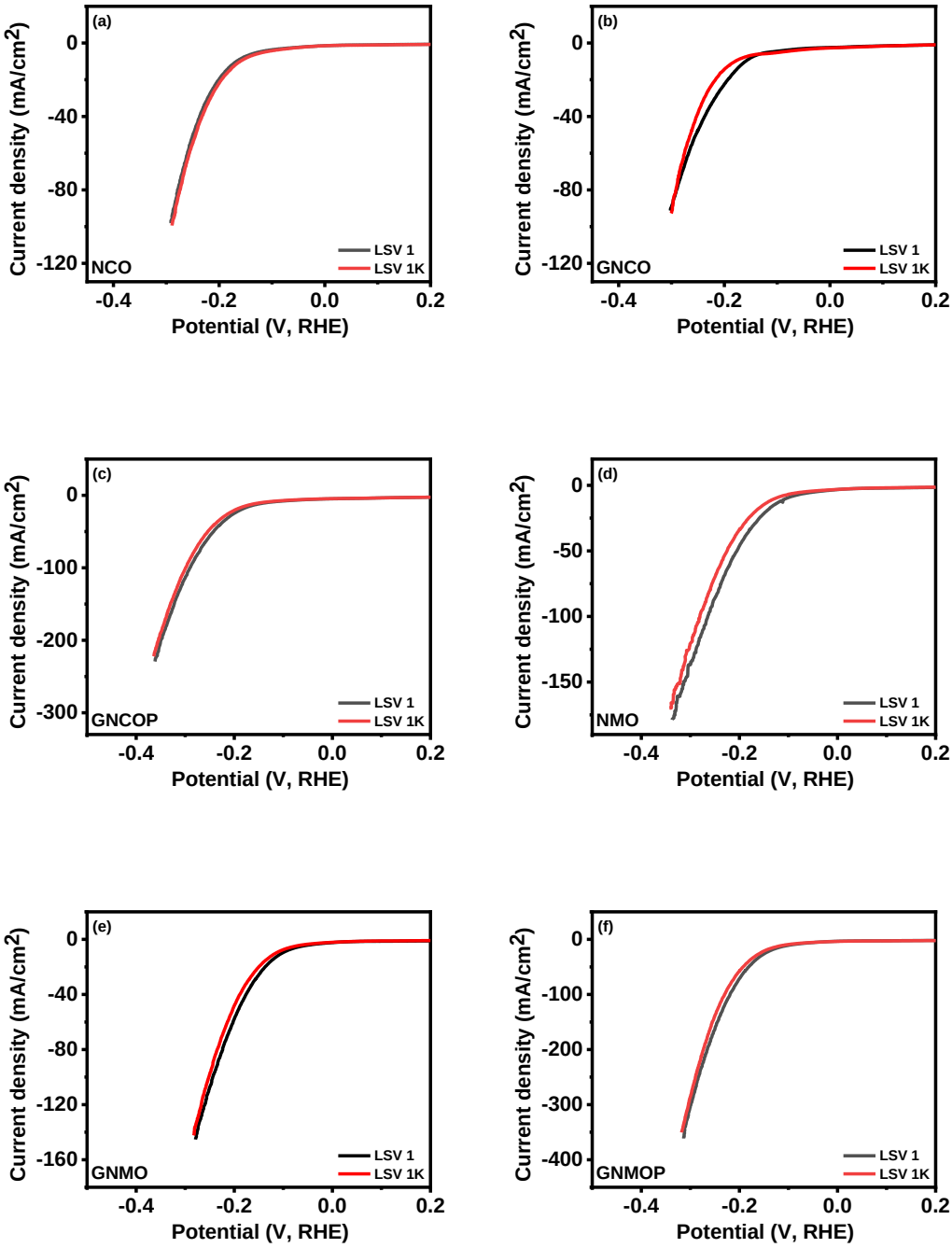
(a)
NCO
LSV 1
LSV 1K
Current density (mA/cm2)
Potential (V, RHE)
(b)
GNCO
(c)
GNCOP
(d)
NMO
(e)
GNMO
(f)
GNMOP

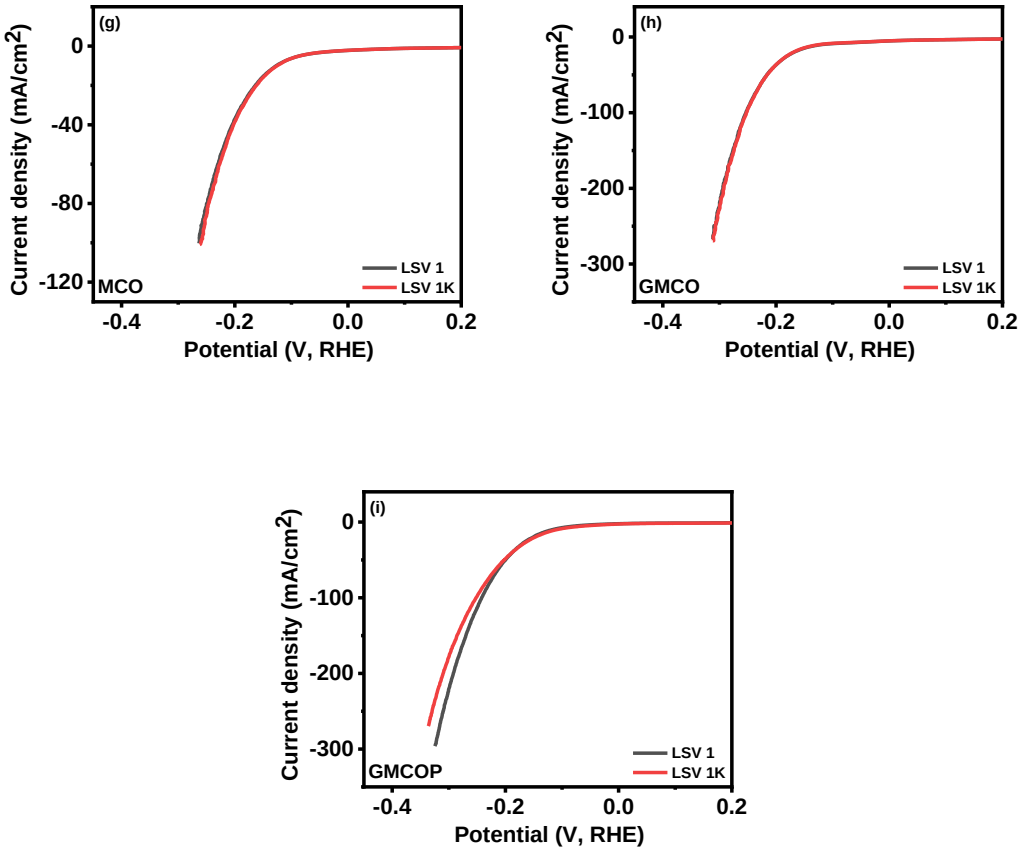

Figure 3.16: 1 vs 1k HER polarization curves of all electrodes.

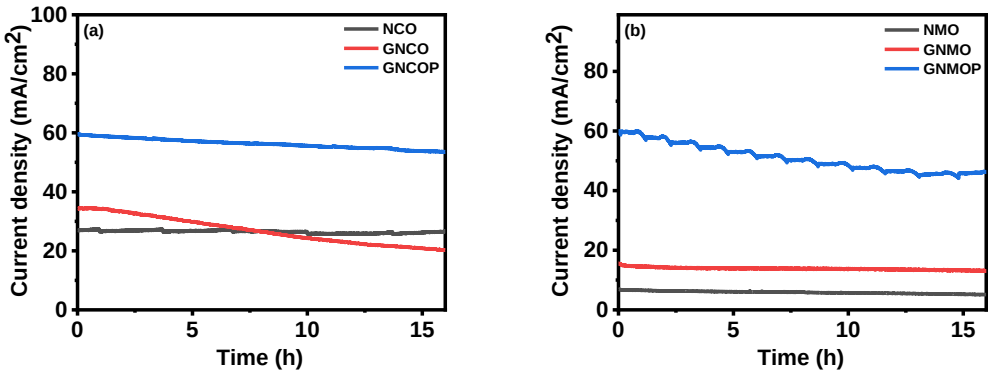

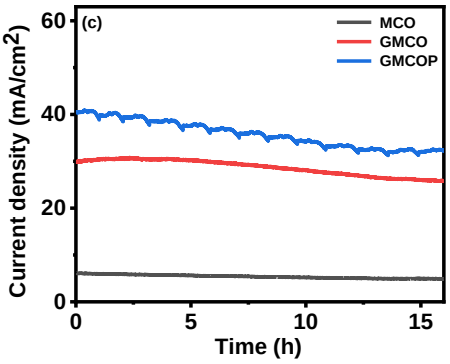

Figure 3.17: CA curves of all electrodes at 1.6 V (V, RHE).

3.2.2. Electrocatalytic properties for electrolyzyer devices

Based on the excellent OER and HER electrocatalytic activities and stable performances of the GNCOP, GNMOP, and GMCOP ternary composite-based electrodes, practical electrolyzers coupled with the electrocatalysts of (GNCOP/GNCOP), (GNMOP/GNMOP), (GMCOP/GMCOP) as cathode/anode were assembled in 1 M KOH electrolyte.

For the assessment of the electrolyzer devices' activity and stability, several measurements were conducted in the 2-electrode system (**Figure 3.18-20)**. LSV measurements were conducted in the range of 1.4-2.2 V. To achieve the current density of 10 mA/cm^2, 1.74, 1.76, and 1.75 V was required for the GNCOP, GNMOP, and GMCOP devices. Also, the Nyquist plot displayed the impedance decrease of each electrolyzer with increasing potential. Moreover, the two-electrode electrolyzer showed robust durability with little deviation between LSV 1 and LSV 1k. Also, excellent long-term stability was recorded by CA measurements, which shows the stable performance

at a high current density for 24 h.

These results show that the combination of rGO and PANI with binary transition metal oxide as a composite form improved the electrocatalytic properties. Consequently, ternary composite electrodes showed good performance in the 3-electrode system as well as electrolyzer devices displayed high activity and stable performances.

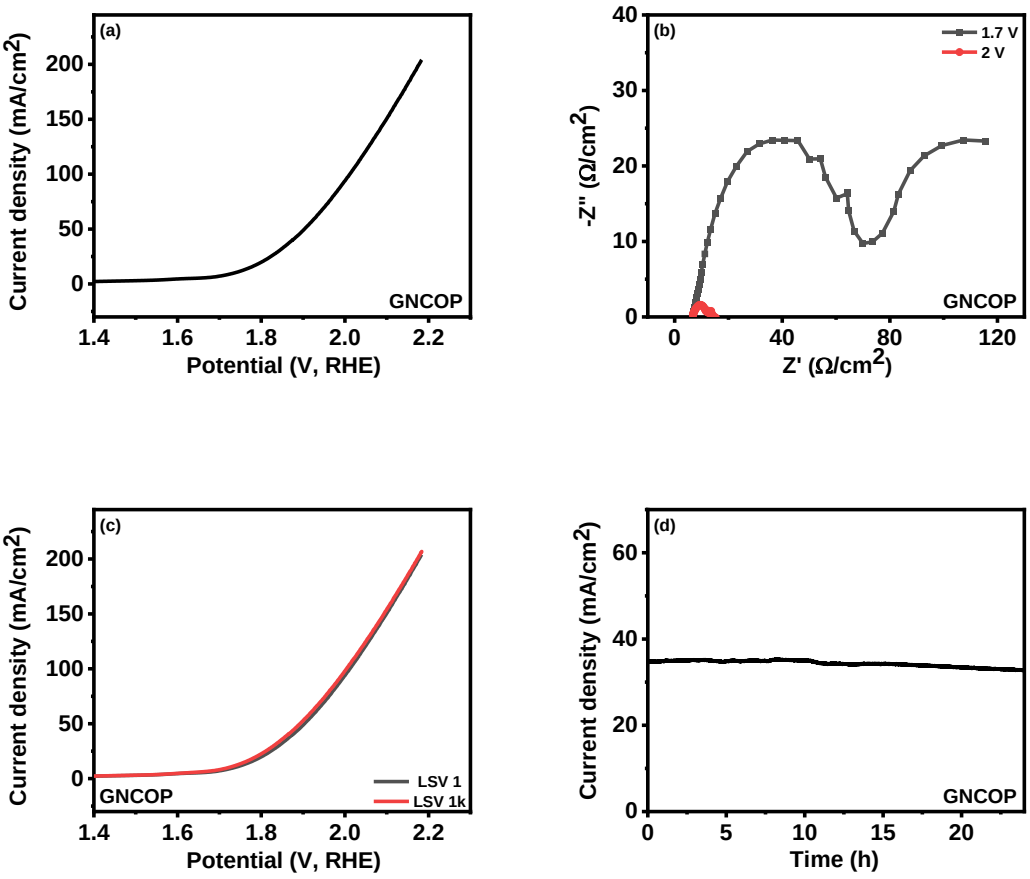

Figure 3.18: (a) Polarization curve, (b) the Nyquist plot at 1.7 and 2 V, (c) 1 vs 1k polarization curves, (d) CA curve for GNCOP electrode using two-electrode water electrolyzer configuration.

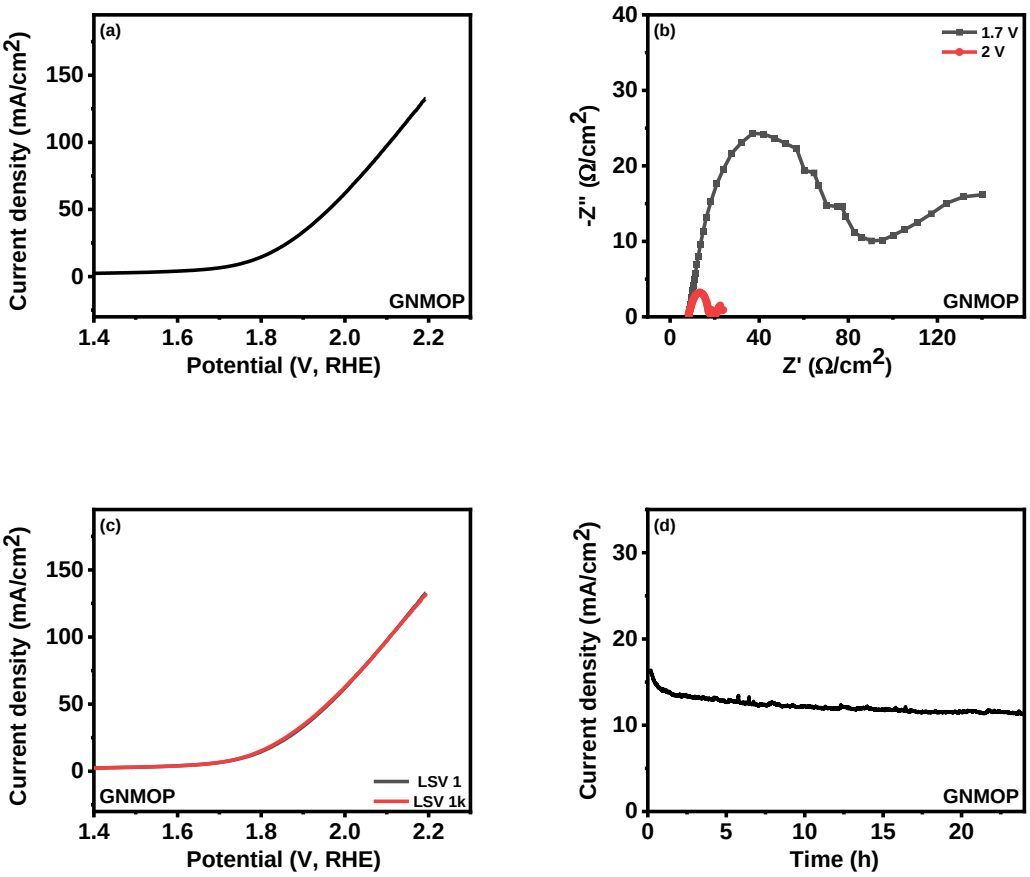

Figure 3.19: (a) Polarization curve, (b) the Nyquist plot at 1.7 and 2 V, (c) 1 vs 1k polarization curves, (d) CA curve for GNMOP electrode using two-electrode water electrolyzer configuration.

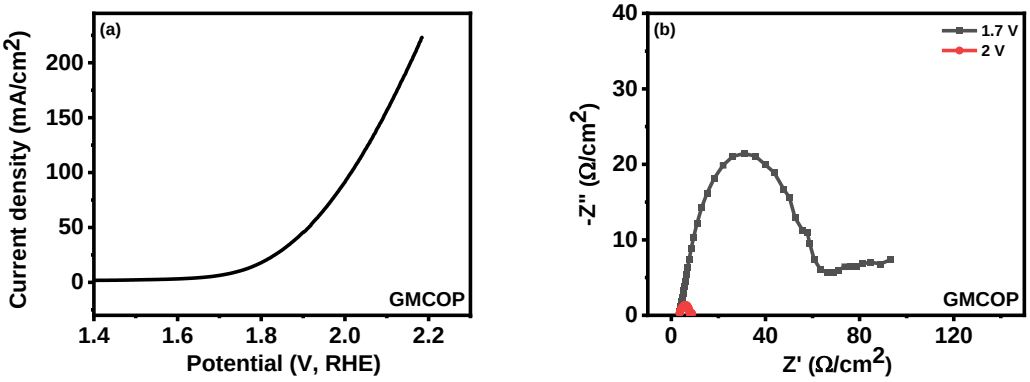

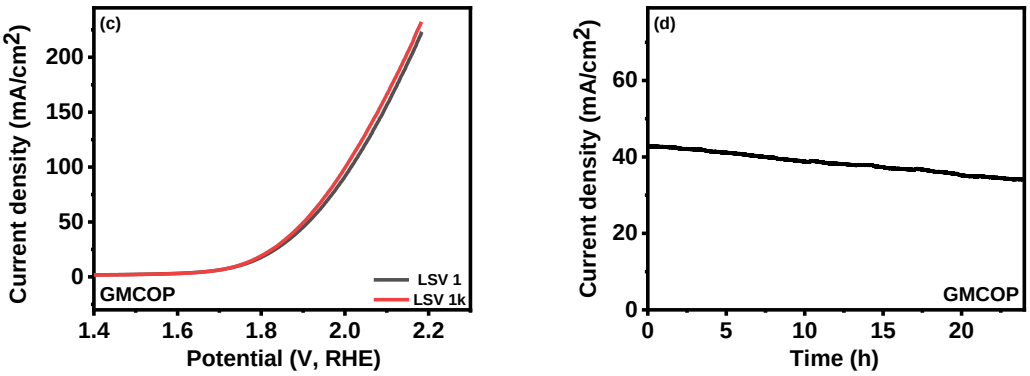

Figure 3.20: (a) Polarization curve, (b) the Nyquist plot at 1.7 and 2 V, (c) 1 vs 1k polarization curves, (d) CA curve for GMCOP electrode using two-electrode water electrolyzer configuration.

3.2.3. Supercapacitive properties

The supercapacitive behavior of all electrodes was investigated through CV and GCD in 3 M KOH. In **Figure 3.21**, various CV curves of as-prepared electrodes were presented, with scan rates ranging from 2-300 mV/s. A pair of peaks was observed from all curves, which indicates the oxidation and reduction peaks, respectively. This non-symmetric behavior suggests the pseudocapacitive type characteristic of supercapacitors.

Figure 3.22 shows the Randles–Sevcik plots of all samples. The increase of scan rate from 2-300 mV/s led to the anodic (I_{pa}) and cathodic (I_{pc}) peak current density, respectively. It also displayed linear behavior as the square root of the scan rate increased. These results were due to the quasi-reversible and rapid redox reaction at the interface between electrode-electrolyte [54–56]. In addition, an increase of anodic and

cathodic peaks towards positive and negative directions suggests that the as-prepared materials have great reversibility with low resistance, and also indicates the contribution of the diffusion-controlled faradic reaction for the charge transfer.

To examine the charge storage mechanism of all electrodes, the following equation was utilized (3.2) [57]:

$$i = av^{b} \quad (3.2)$$

where i is the peak current density, v is a scan rate, and a and b are variable parameters of all materials. Depending on the value of b, the charge storage contribution can be determined. When b is 0.5, charges are only stored by diffusion-controlled faradic redox reaction. Furthermore, capacitive mechanism is only utilized when b is 1.

In **Figure 3.23,** the b value of all electrodes is 0.8, 0.78, 0.77, 0.62, 0.61, 0.64, 0.63, 0.64, and 0.61 for NCO, GNCO, GNCOP, NMO, GNMO, GNMOP, MCO, GMCO, and GMCOP electrodes, respectively. These results indicate that all electrodes have a hybrid charge storage mechanism combined with diffusion and capacitance effects. For a detailed understanding of the charge storage mechanism, the following equation was employed (3.3) [57]:

$$i = k_1 v + k_2 v^{1/2} \quad (3.3)$$

where k_1v is the capacitive contribution and $k_2v^{1/2}$ is the diffusion-controlled faradic redox reaction contribution.

Figure 3.24 shows the capacitance and diffusion contribution of all samples at scan rates of 10 and 100 mV/s, respectively. At the lower scan rate of 10 mV/s, the capacitance and diffusion effects were 40 and 60%, 43 and 57%, 45 and 55%, 7 and 93%, 17 and 83%, 14 and 86%, 14 and 86%, 14 and 86%, and 12 and 88% for NCO, GNCO, GNCOP, NMO, GNMO, GNMOP, MCO, GMCO, and GMCOP electrodes,

respectively. On the other hand, at a high scan rate of 100 mV/s, these capacitance and diffusion contributions were 68 and 32%, 70 and 30%, 72 and 28%, 20 and 80%, 39 and 61%, 35 and 65%, 34 and 66%, 33 and 67%, and 31 and 69% for NCO, GNCO, GNCOP, NMO, GNMO, GNMOP, MCO, GMCO, and GMCOP electrodes, respectively. An increase in the capacitance effect was observed at a higher scan rate of 100 mV/s compared to a lower scan rate of 10 mV/s, which affected energy storage properties of all electrodes. To see the detailed information about the specific capacitance (C) of all electrodes, the following equation was utilized (3.4) [58]:

$$\mathrm{C\ (F/g)} = \frac{\mathrm{A}}{\mathrm{v} \times \Delta V \times \mathrm{m}} \tag{3.4}$$

Where A is the area under the CV graph (A), V is the working potential (V), v is the scan rate (mV/s), and m is the weight of all active materials (g).

Figure 3.25 shows a specific capacitance of 206, 261, 243, 211, 285, 248, 145, 189, 205 F/g for the NCO, GNCO, GNCOP, NMO, GNMO, GNMOP, MCO, GMCO, and GMCOP electrodes respectively at a current density of 2 mV/s. The specific capacitance of all electrodes decreased as the scan rate increased. This is because the diffusion-controlled faradic reaction mainly takes place at the low scan rate, which facilitates the electrolyte moving into the deep inner part of the material, resulting in higher specific capacitance. On the other hand, at a higher scan rate, more capacitance effect takes place on the outer surface of the material compared to a lower scan rate, resulting in lower energy storage performance [59]. The GCD measurements were conducted using all electrodes in the range of 0.5-30 A/g.

Figure 3.26 shows the GCD curves of all electrodes. Non-linear behavior of the GCD curves was observed from all electrodes, suggesting that all electrodes are of the pseudo capacitive type, which is in good agreement with the CV measurements. In more

detail, the discharge curve with nonlinear shape can be divided into three sections: a rapid voltage drop in the beginning, then a voltage plateau followed by a fast voltage drop at the end. This phenomenon is due to the internal resistance, the occurrences of faradaic redox reaction between electrode materials and electrolyte, and the presence of electric double layer capacitors, respectively [60]. According to the following equation, the specific capacitance of all electrodes was calculated (3.5) [61]:

$$C\ (F/g) = \frac{I \times \Delta t}{\Delta V \times m} \tag{3.5}$$

where I is the discharge current range (A), Δt is the discharge time range (s), ΔV is the working potential range (V), and m is the mass (g) of each material.

Figure 3.27 shows a specific capacitance of 80, 94, 68, 54, 63, 44, 21, 51, 53 F/g for NCO, GNCO, GNCOP, NMO, GNMO, GNMOP, MCO, GMCO, and GMCOP electrodes respectively at 0.5 A/g.

Figure 3.28 exhibited the Ragone plot showing the relationship between energy (E) and power density (P). The energy and power density of all electrodes were obtained by the following equations (3.6-7) [62]:

$$E\ (Wh/kg) = \frac{1}{2} \times C \times V^2 \tag{3.6}$$

$$P\ (W/kg) = \frac{E}{t} \tag{3.7}$$

The maximum energy and power density of all electrodes was seen in **Table 3.1**.

The stability of the supercapacitor electrodes was also assessed, as shown in **Figure 3.29**. The 7,000 charge-discharge processes were carried out using GCD measurements. Stable cycling performance was observed from all electrodes, and shows a high retention of 93, 92, 72, 98, 88, 96, 97, 82, and 97% for the NCO, GNCO, GNCOP, NMO, GNMO, GNMOP, MCO, GMCO, and GMCOP electrodes, respectively. In

addition, a high Coulombic efficiency of average 99% was achieved for all as-prepared electrodes.

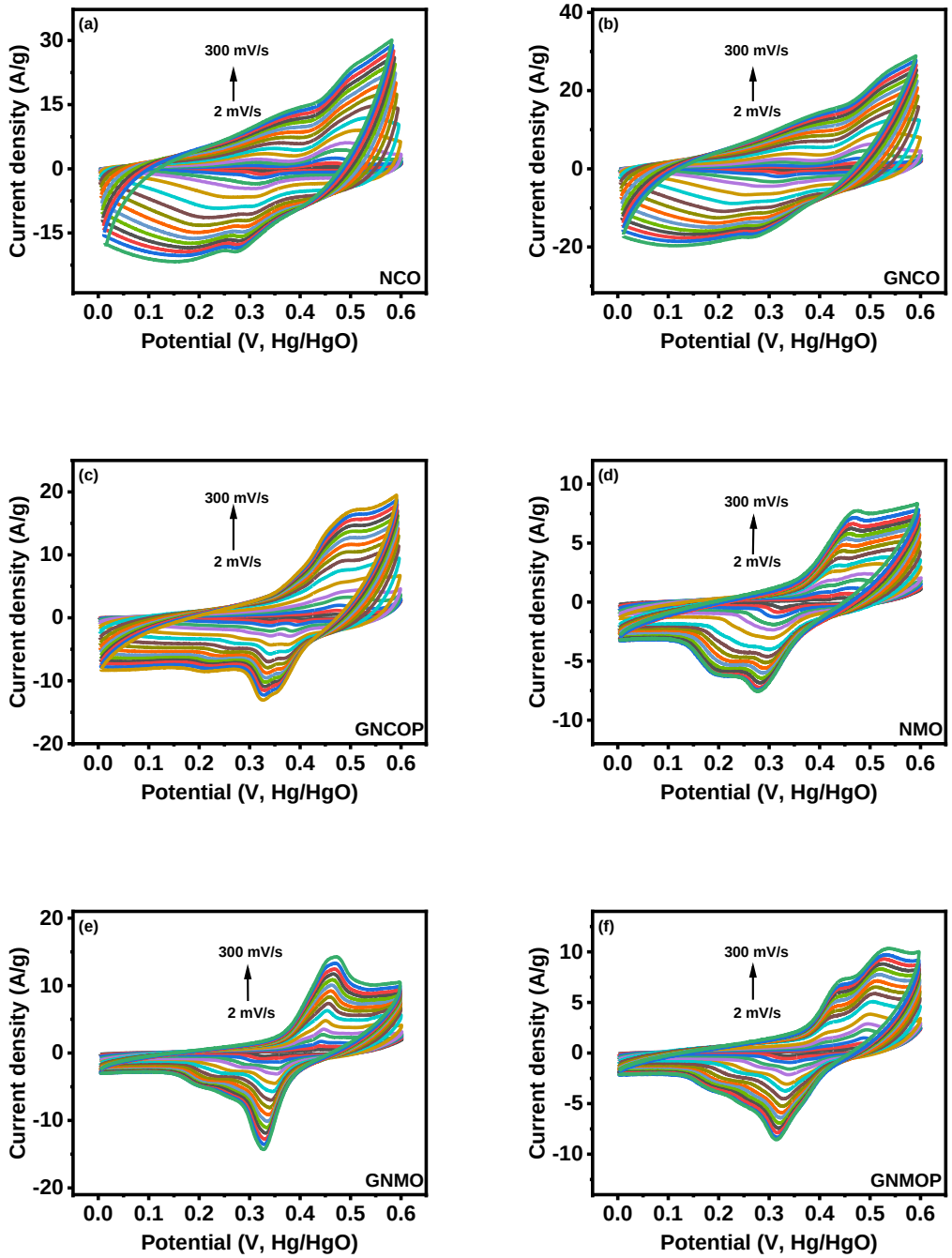

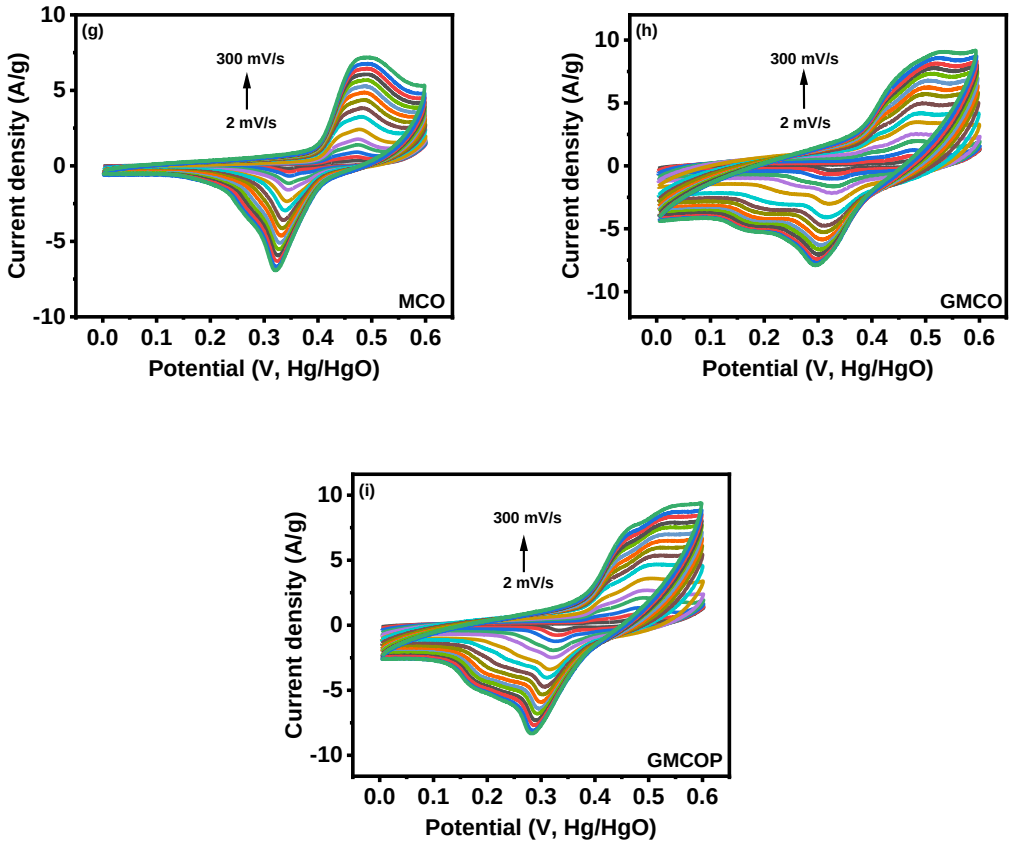

Figure 3.21: CV curves of all electrodes at the scan rate from 2-300 mV/s.

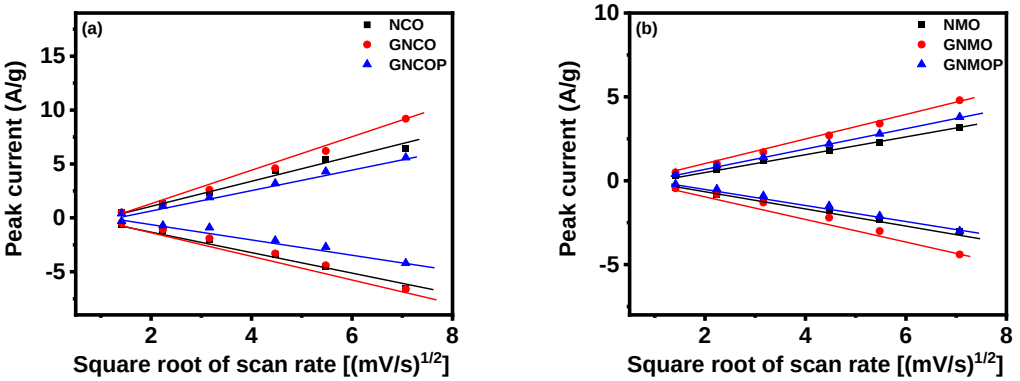

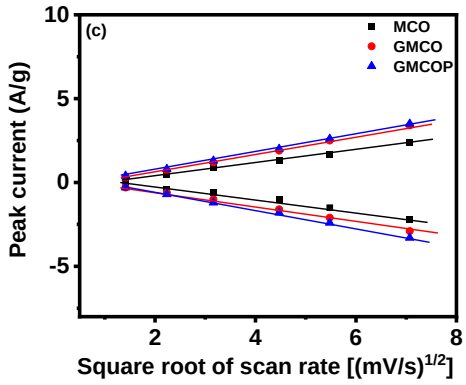

Figure 3.22: Peak current density vs (scan rate)$^{1/2}$ plots for all electrodes.

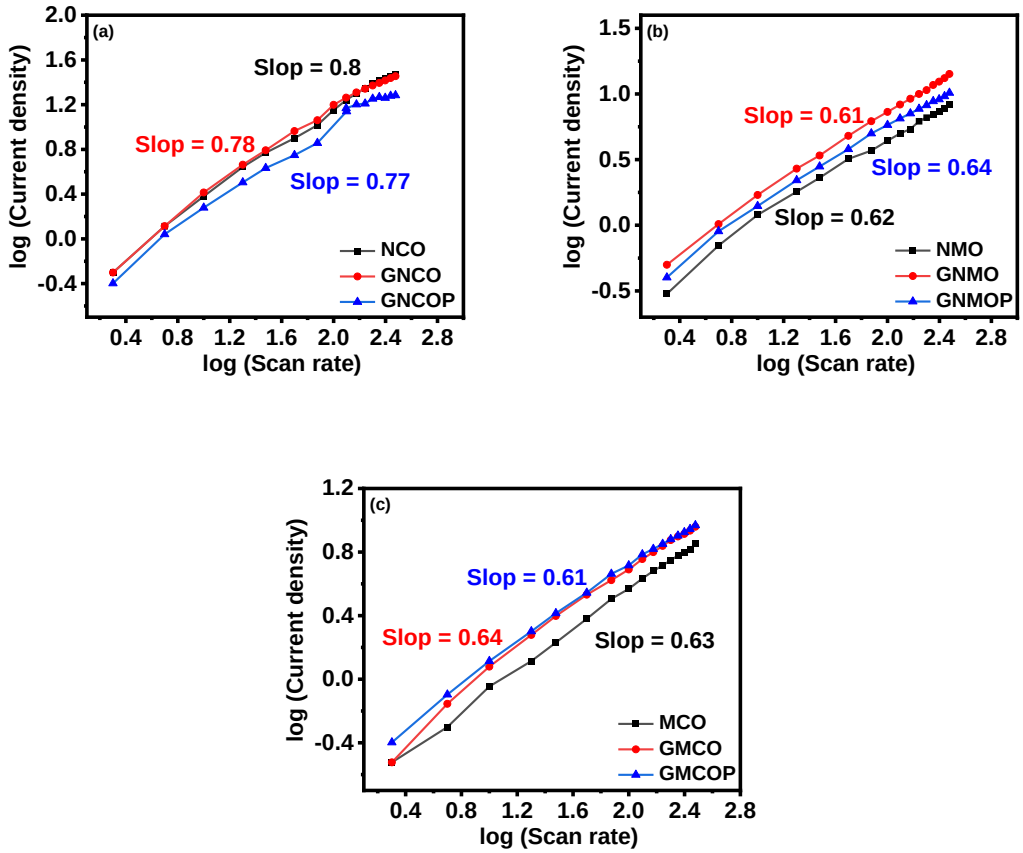

Figure 3.23: Log (current density) vs log (scan rate) plots for all electrodes.

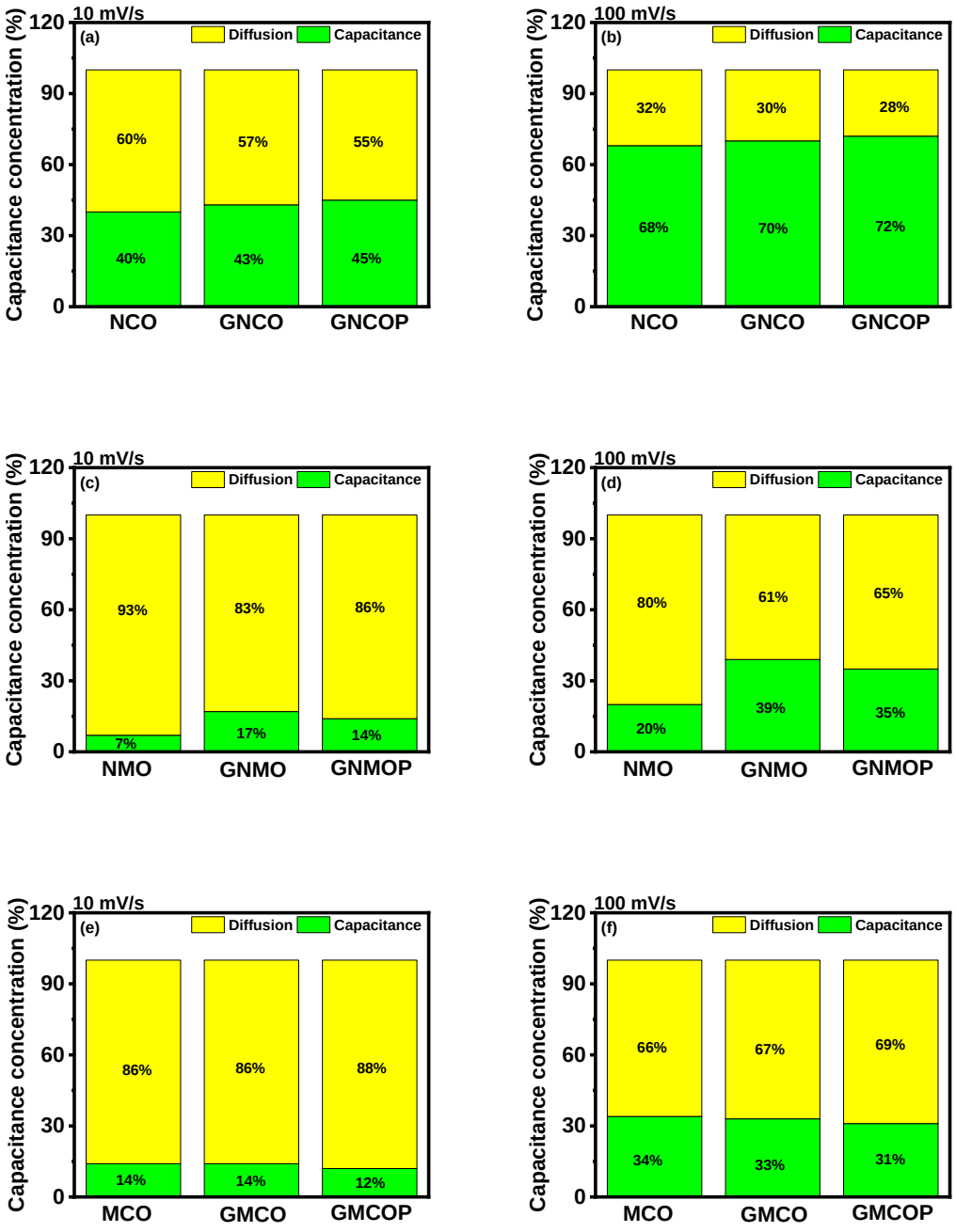

Figure 3.24: Diffusion and capacitive effects for all electrodes at the 10 and 100 mV/s.

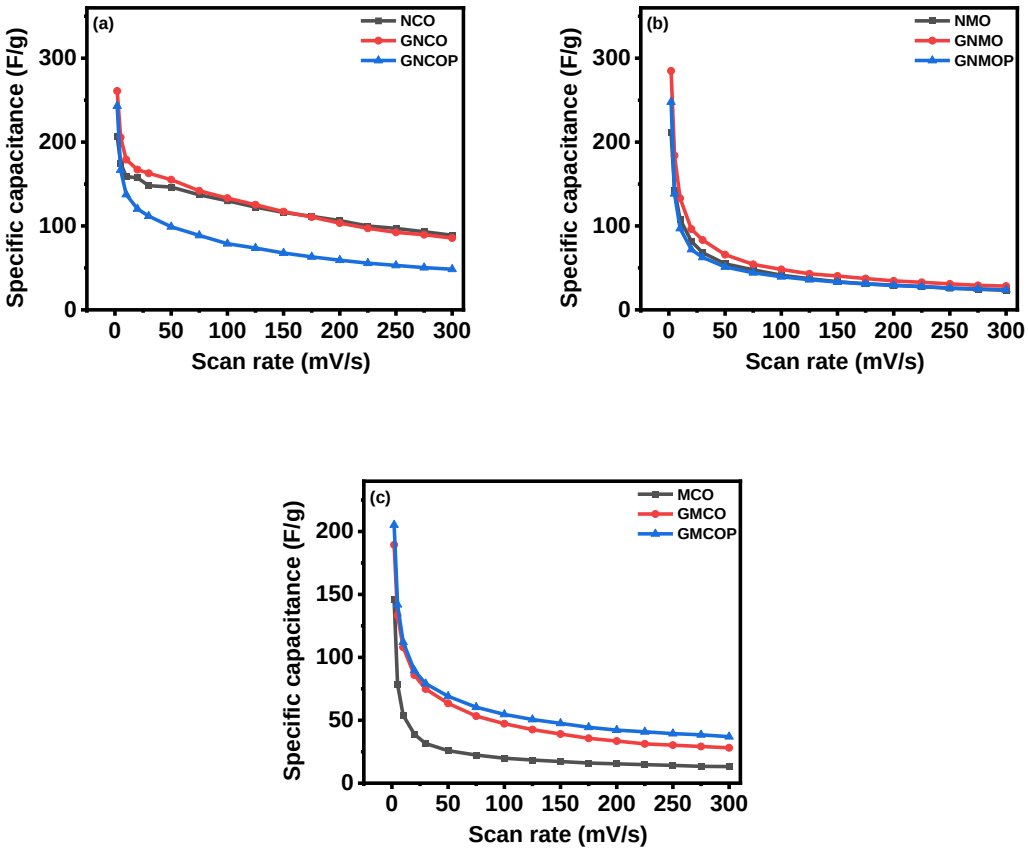

Figure 3.25: A specific capacitance of all electrodes at various scan rate (2-300 mV/s).

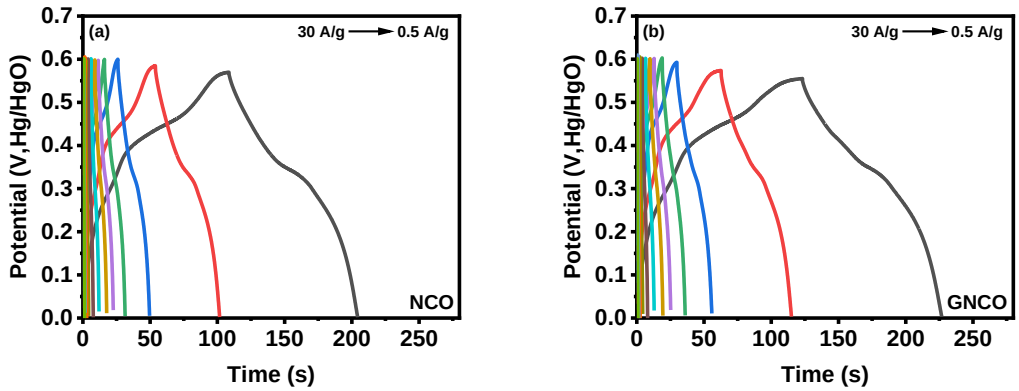

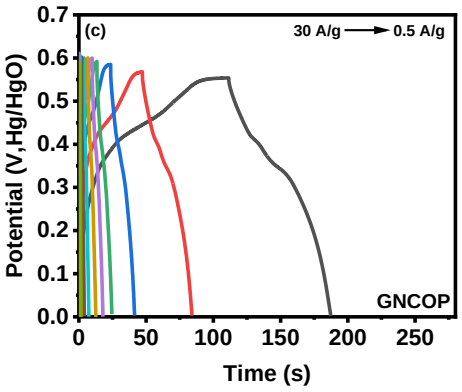
(c)
30 A/g → 0.5 A/g
GNCOP
Potential (V,Hg/HgO)
Time (s)

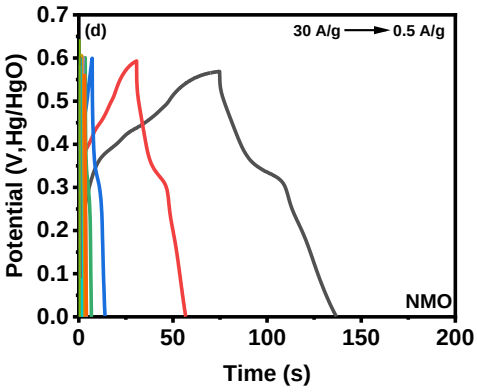
(d)
30 A/g → 0.5 A/g
NMO
Potential (V,Hg/HgO)
Time (s)

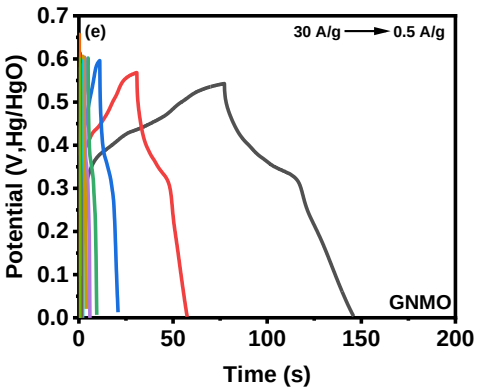
(e)
30 A/g → 0.5 A/g
GNMO
Potential (V,Hg/HgO)
Time (s)

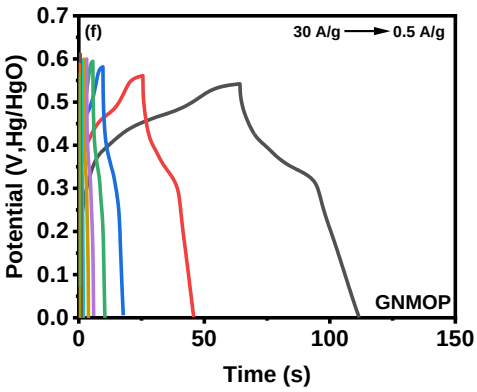
(f)
30 A/g → 0.5 A/g
GNMOP
Potential (V,Hg/HgO)
Time (s)

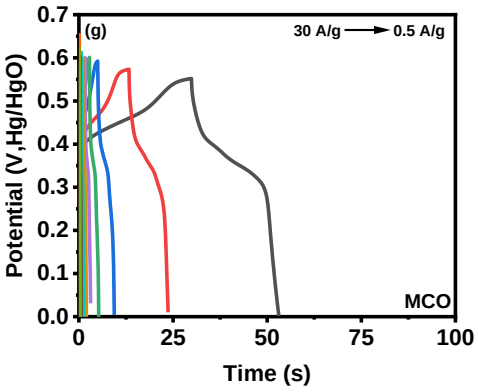
(g)
30 A/g → 0.5 A/g
MCO
Potential (V,Hg/HgO)
Time (s)

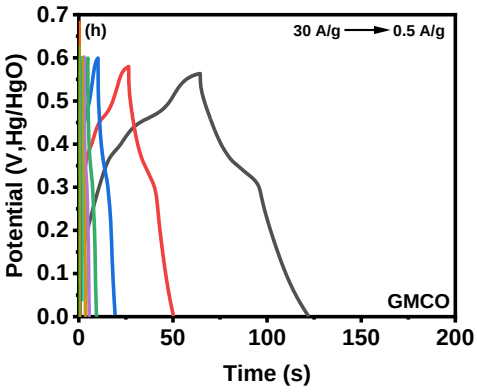
(h)
30 A/g → 0.5 A/g
GMCO
Potential (V,Hg/HgO)
Time (s)

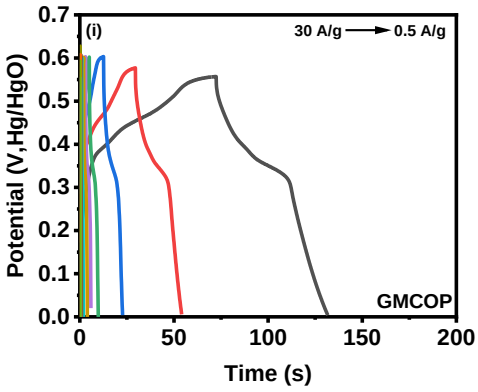

Figure 3.26: GCD curves of all electrodes at the current density from 0.5-30 A/g.

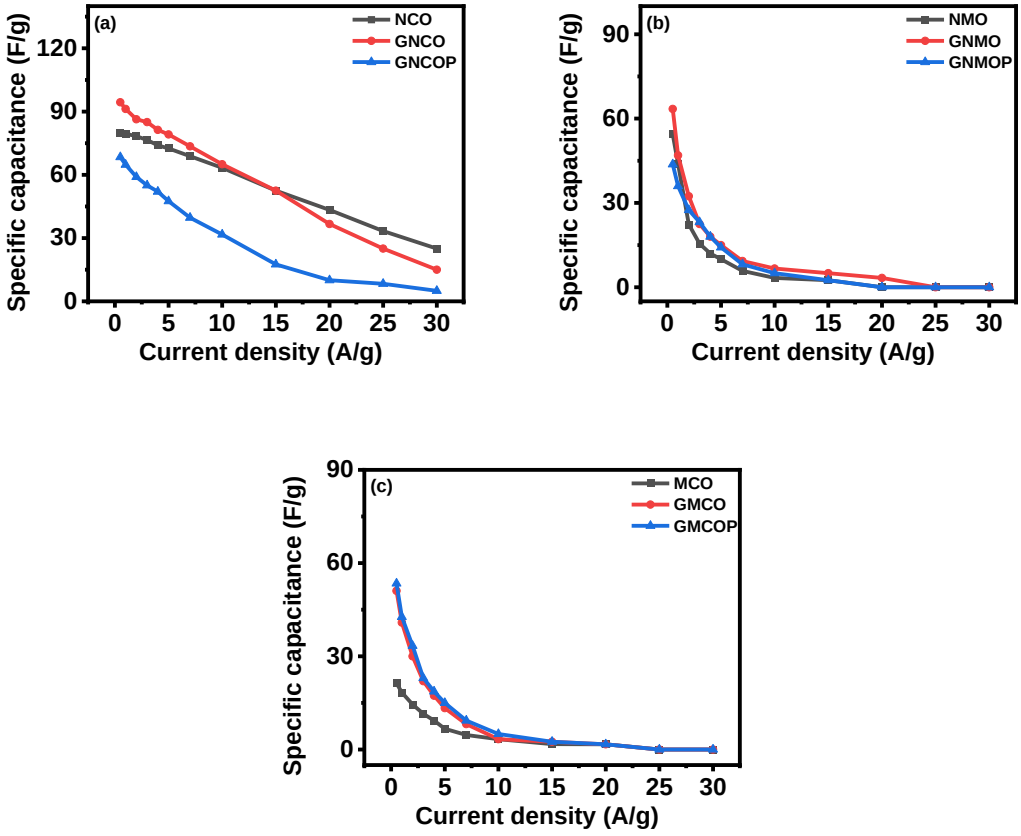

Figure 3.27: A specific capacitance of all electrodes at various current density (0.5-30 A/g).

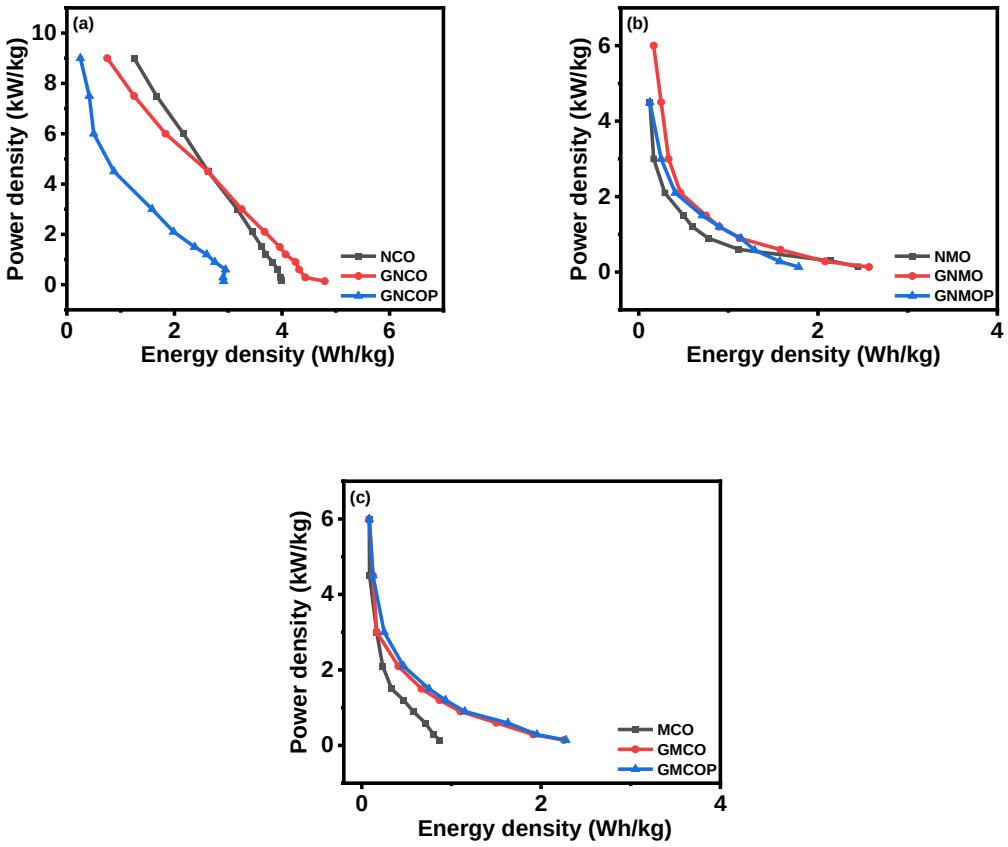

Figure 3.28: The Ragone plot of all electrodes.

Table 3.1: The maximum energy and power density of all electrodes.

Sample Name	Maximum energy density (Wh/kg)	Maximum Power density (W/kg)
NCO	3.98	9,000
GNCO	4.79	9,000
GNCOP	2.9	9,000
NMO	2.4	4,500
GNMO	2.57	6,000
GNMOP	1.8	4,500
MCO	0.87	6,000
GMCO	2.2	6,000
GMCOP	2.3	6,000

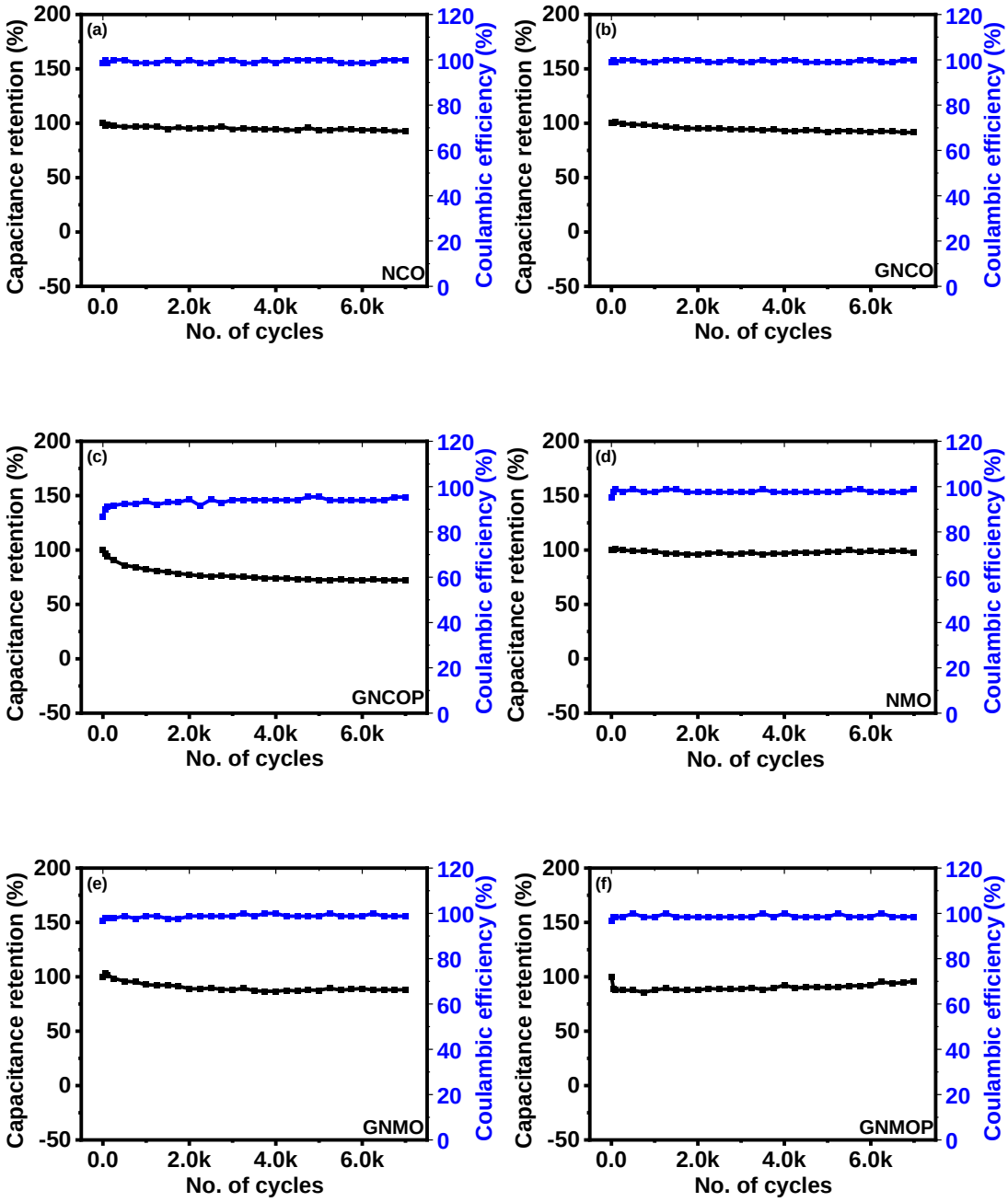
(a)
NCO
(b)
GNCO
(c)
GNCOP
(d)
NMO
(e)
GNMO
(f)
GNMOP
Capacitance retention (%)
Coulambic efficiency (%)
No. of cycles
200
150
100
50
0
-50
120
100
80
60
40
20
0
0.0
2.0k
4.0k
6.0k

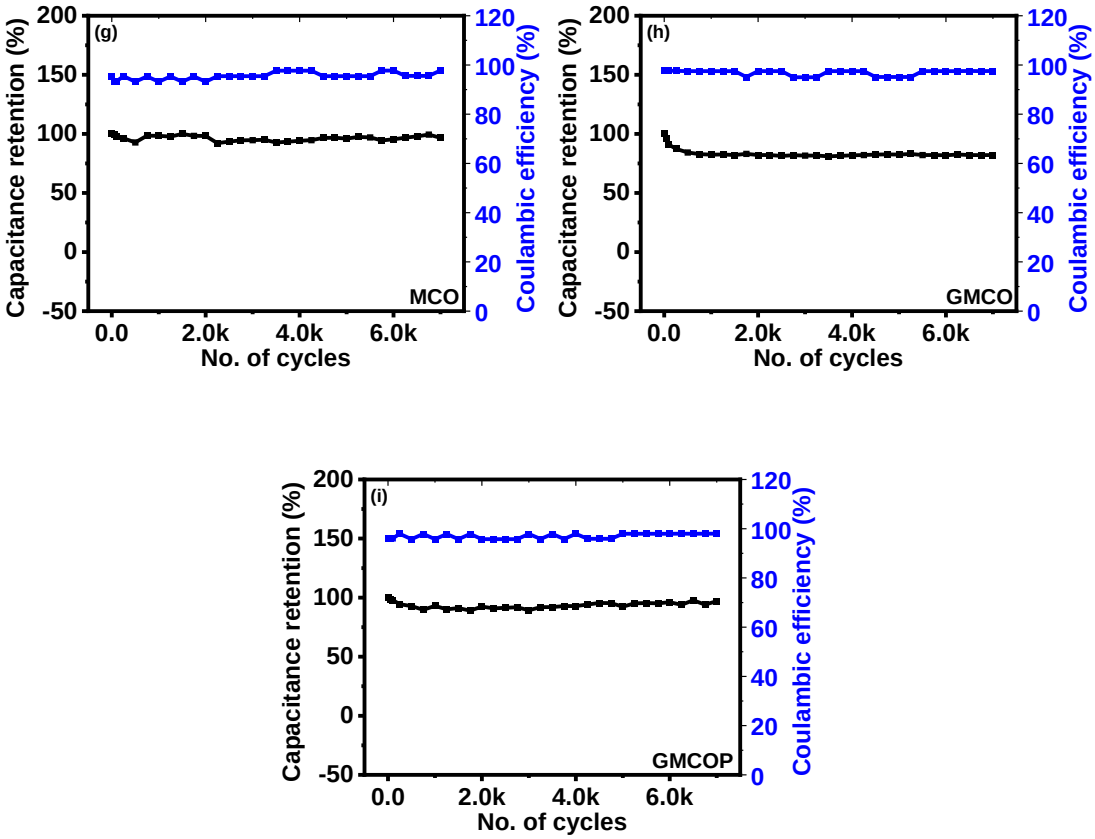

Figure 3.29: Capacitance retention and coulombic efficiency of all electrodes up to 7,000 charge-discharge cycles.

CHAPTER IV

CONCLUSION

Ternary composite materials were prepared via successive hydrothermal synthesis and polymerization of aniline. All prepared materials possess a uniform rod-like structure, and these materials were utilized as electrocatalysts for the water splitting reaction and as the electrode for a supercapacitor. Ternary composite materials showed advanced electrocatalytic properties compared to binary transition metal oxide and binary composite materials. GNCOP, GNMOP, GMCOP electrodes showed not only lower OER overpotential of 342, 340, and 382 mV, but also lower HER overpotential of 134, 96, and 117 mV at the current density of 10 mA/cm^2.

Considering the low overpotential of ternary composite materials, a two-electrode electrolyzer was configured by two parallel electrodes (GNCOP// GNCOP), (GNMOP// GNMOP), and (GMCOP// GMCOP). These electrolyzers delivered the 1.74, 1.76, and 1.75 V to generate the current density of 10 mA/cm^2, as well as showed a stable performance at the high current density over 24 h. The specific capacitance of ternary composite electrodes was in the range of 145-285 F/g at a scan rate of 2 mV/s. Also, the energy and power density of these electrodes was in the range 0.87 to 4.79 Wh/kg and 4,500 to 9,000 W/kg, respectively. Additionally, all ternary composites-based electrodes showed high capacitance retention with average 99% coulombic efficiency up to 7,000 cycles.

REFERENCES

[1] X. Zou, Y. Zhang, Noble metal-free hydrogen evolution catalysts for water splitting, Chemical Society Reviews. 44 (2015) 5148–5180. https://doi.org/10.1039/c4cs00448e.

[2] J.S. Lee, S.T. Kim, R. Cao, N.S. Choi, M. Liu, K.T. Lee, J. Cho, Metal-air batteries with high energy density: Li-air versus Zn-air, Advanced Energy Materials. 1 (2011) 34–50. https://doi.org/10.1002/aenm.201000010.

[3] J. Wang, J. Liu, B. Zhang, F. Cheng, Y. Ruan, X. Ji, K. Xu, C. Chen, L. Miao, J. Jiang, Stabilizing the oxygen vacancies and promoting water-oxidation kinetics in cobalt oxides by lower valence-state doping, Nano Energy. 53 (2018) 144–151. https://doi.org/https://doi.org/10.1016/j.nanoen.2018.08.022.

[4] C. Li, J.B. Baek, Recent Advances in Noble Metal (Pt, Ru, and Ir)-Based Electrocatalysts for Efficient Hydrogen Evolution Reaction, ACS Omega. 5 (2020) 31–40. https://doi.org/10.1021/acsomega.9b03550.

[5] SP. Keerthana, R. Yuvakkumar, G. Ravi, M. Pannipara, A.G. Al-Sehemi, D. Velauthapillai, Cobalt Vanadium Oxide Nanoclusters for Oxygen Evolution Reaction, ECS Journal of Solid State Science and Technology. 10 (2021) 071003. https://doi.org/10.1149/2162-8777/ac0e0f.

[6] J. He, M. Wang, W. Wang, R. Miao, W. Zhong, S.Y. Chen, S. Poges, T. Jafari, W. Song, J. Liu, S.L. Suib, Hierarchical Mesoporous NiO/MnO2@PANI Core-Shell Microspheres, Highly Efficient and Stable Bifunctional Electrocatalysts

for Oxygen Evolution and Reduction Reactions, ACS Applied Materials and Interfaces. 9 (2017) 42676–42687. https://doi.org/10.1021/acsami.7b07383.

[7] N. Nitta, F. Wu, J.T. Lee, G. Yushin, Li-ion battery materials: Present and future, Materials Today. 18 (2015) 252–264. https://doi.org/10.1016/j.mattod.2014.10.040.

[8] Y. Wang, Y. Song, Y. Xia, Electrochemical capacitors: Mechanism, materials, systems, characterization and applications, Chemical Society Reviews. 45 (2016) 5925–5950. https://doi.org/10.1039/c5cs00580a.

[9] J. Choi, C. Zequine, S. Bhoyate, W. Lin, X. Li, P. Kahol, R. Gupta, Waste Coffee Management: Deriving High-Performance Supercapacitors Using Nitrogen-Doped Coffee-Derived Carbon, C (Basel). 5 (2019). https://doi.org/10.3390/c5030044.

[10] L. Zhang, X. Hu, Z. Wang, F. Sun, D.G. Dorrell, A review of supercapacitor modeling, estimation, and applications: A control/management perspective, Renewable and Sustainable Energy Reviews. 81 (2018) 1868–1878. https://doi.org/https://doi.org/10.1016/j.rser.2017.05.283.

[11] H. Wang, L. Pilon, Accurate simulations of electric double layer capacitance of ultramicroelectrodes, Journal of Physical Chemistry C. 115 (2011) 16711–16719. https://doi.org/10.1021/jp204498e.

[12] S. Bhoyate, P.K. Kahol, R.K. Gupta, Nanostructured materials for supercapacitor applications, SPR Nanoscience. 5 (2019) 1–29. https://doi.org/10.1039/9781788013871-00001.

[13] J. Choi, T. Wixson, A. Worsley, S. Dhungana, S.R. Mishra, F. Perez, R.K. Gupta, Pomegranate: An eco-friendly source for energy storage devices, Surface and Coatings Technology. 421 (2021). https://doi.org/10.1016/j.surfcoat.2021.127405.

[14] Y. Jiang, J. Liu, Definitions of Pseudocapacitive Materials: A Brief Review, Energy and Environmental Materials. 2 (2019) 30–37. https://doi.org/10.1002/eem2.12028.

[15] D. Yan, Y. Li, Y. Liu, R. Zhuo, B. Geng, Z. Wu, J. Wang, P. Ren, P. Yan, Design and influence of mass ratio on supercapacitive properties of ternary electrode material reduced graphene oxide@MnO2@ poly(3,4-ethylenedioxythiophene)-poly(styrene sulfonate), Electrochimica Acta. 169 (2015) 317–325. https://doi.org/10.1016/j.electacta.2015.04.078.

[16] A. Afif, S.M. Rahman, A. Tasfiah Azad, J. Zaini, M.A. Islam, A.K. Azad, Advanced materials and technologies for hybrid supercapacitors for energy storage – A review, Journal of Energy Storage. 25 (2019). https://doi.org/10.1016/j.est.2019.100852.

[17] H. Gao, F. Xiao, C.B. Ching, H. Duan, High-Performance Asymmetric Supercapacitor Based on Graphene Hydrogel and Nanostructured MnO2, ACS Applied Materials & Interfaces. 4 (2012) 2801–2810. https://doi.org/10.1021/am300455d.

[18] J. Hao, H. Liu, S. Han, J. Lian, MoS2Nanosheet-Polypyrrole Composites Deposited on Reduced Graphene Oxide for Supercapacitor Applications, ACS

Applied Nano Materials. 4 (2021) 1330–1339. https://doi.org/10.1021/acsanm.0c02899.

[19] Y. Zhang, L. Li, H. Su, W. Huang, X. Dong, Binary metal oxide: Advanced energy storage materials in supercapacitors, Journal of Materials Chemistry A. 3 (2015) 43–59. https://doi.org/10.1039/c4ta04996a.

[20] K. Allado, M. Liu, A. Jayapalan, D. Arvapalli, K. Nowlin, J. Wei, Binary MnO2/Co3O4metal oxides wrapped on superaligned electrospun carbon nanofibers as binder free supercapacitor electrodes, Energy and Fuels. 35 (2021) 8396–8405. https://doi.org/10.1021/acs.energyfuels.1c00556.

[21] Q. Deng, M. Wang, Z. Peng, Z. Liu, H. Fan, Y. Zhang, Ultrafast Li+ diffusion kinetics enhanced by cross-stacked nanosheets loaded with Co3O4@NiO nanoparticles: Constructing superstructure to enhance Li-ion half/full batteries, Journal of Colloid and Interface Science. 585 (2021) 51–60. https://doi.org/10.1016/j.jcis.2020.11.052.

[22] M.R. Tarasevich, B.N. Efremov, S. Trasatti, Electrodes of conductive metallic oxides, part A, Elsevier, USA. (1982) 227.

[23] B.R. Wiston, M. Ashok, Microwave-assisted synthesis of cobalt-manganese oxide for supercapacitor electrodes, Materials Science in Semiconductor Processing. 103 (2019) 104607. https://doi.org/https://doi.org/10.1016/j.mssp.2019.104607.

[24] F. Xiang, X. Zhou, X. Yue, Q. Hu, Q. Zheng, D. Lin, An oxygen-deficient cobalt-manganese oxide nanowire doped with P designed for high performance

asymmetric supercapacitor, Electrochimica Acta. 379 (2021) 138178. https://doi.org/https://doi.org/10.1016/j.electacta.2021.138178.

[25] U.J. Chavan, A.A. Yadav, Electrochemical behavior of spray deposited mixed nickel manganese oxide thin films for supercapacitor applications, Journal of Materials Science: Materials in Electronics. 28 (2017) 4958–4964. https://doi.org/10.1007/s10854-016-6148-z.

[26] X. Deng, S. Öztürk, C. Weidenthaler, H. Tüysüz, Iron-Induced Activation of Ordered Mesoporous Nickel Cobalt Oxide Electrocatalyst for the Oxygen Evolution Reaction, ACS Applied Materials and Interfaces. 9 (2017) 21225–21233. https://doi.org/10.1021/acsami.7b02571.

[27] P. Ahuja, S. Kumar Ujjain, R.K. Sharma, G. Singh, Enhanced supercapacitor performance by incorporating nickel in manganese oxide, n.d.

[28] C. Zhu, D. Wen, S. Leubner, M. Oschatz, W. Liu, M. Holzschuh, F. Simon, S. Kaskel, A. Eychmüller, Nickel cobalt oxide hollow nanosponges as advanced electrocatalysts for the oxygen evolution reaction, Chemical Communications. 51 (2015) 7851–7854. https://doi.org/10.1039/c5cc01558h.

[29] W.-L. Hong, L.-Y. Lin, Design of nickel cobalt oxide and nickel cobalt oxide@nickel molybdenum oxide battery-type materials for flexible solid-state battery supercapacitor hybrids, Journal of Power Sources. 435 (2019) 226797. https://doi.org/https://doi.org/10.1016/j.jpowsour.2019.226797.

[30] R. Elakkiya, G. Maduraiveeran, A three-dimensional nickel–cobalt oxide nanomaterial as an enzyme-mimetic electrocatalyst for the glucose and lactic

acid oxidation reaction, New Journal of Chemistry. 43 (2019) 14756–14762. https://doi.org/10.1039/C9NJ01291E.

[31] M. Govindhan, B. Sidhureddy, A. Chen, High-Temperature Hydrogen Gas Sensor Based on Three-Dimensional Hierarchical-Nanostructured Nickel-Cobalt Oxide, ACS Applied Nano Materials. 1 (2018) 6005–6014. https://doi.org/10.1021/acsanm.8b00835.

[32] Q. Ke, J. Wang, Graphene-based materials for supercapacitor electrodes – A review, Journal of Materiomics. 2 (2016) 37–54. https://doi.org/https://doi.org/10.1016/j.jmat.2016.01.001.

[33] Q. Ke, Y. Liu, H. Liu, Y. Zhang, Y. Hu, J. Wang, Surfactant-modified chemically reduced graphene oxide for electrochemical supercapacitors, RSC Advances. 4 (2014) 26398–26406. https://doi.org/10.1039/C4RA03826F.

[34] Z. Ismail, Green reduction of graphene oxide by plant extracts: A short review, Ceramics International. 45 (2019) 23857–23868. https://doi.org/10.1016/j.ceramint.2019.08.114.

[35] A. Eftekhari, L. Li, Y. Yang, Polyaniline supercapacitors, Journal of Power Sources. 347 (2017) 86–107. https://doi.org/10.1016/j.jpowsour.2017.02.054.

[36] L.-B. Kong, J. Zhang, J.-J. An, Y.-C. Luo, L. Kang, MWNTs/PANI composite materials prepared by in-situ chemical oxidative polymerization for supercapacitor electrode, Journal of Materials Science. 43 (2008) 3664–3669. https://doi.org/10.1007/s10853-008-2586-1.

[37] Y. Fan, H. Chen, Y. Li, D. Cui, Z. Fan, C. Xue, PANI-Co3O4 with excellent

specific capacitance as an electrode for supercapacitors, Ceramics International. 47 (2021) 8433–8440. https://doi.org/10.1016/j.ceramint.2020.11.208.

[38] T. Prasankumar, B.R. Wiston, C.R. Gautam, R. Ilangovan, S.P. Jose, Synthesis and enhanced electrochemical performance of PANI/Fe3O4 nanocomposite as supercapacitor electrode, Journal of Alloys and Compounds. 757 (2018) 466–475. https://doi.org/https://doi.org/10.1016/j.jallcom.2018.05.108.

[39] M.B. Gholivand, H. Heydari, A. Abdolmaleki, H. Hosseini, Nanostructured CuO/PANI composite as supercapacitor electrode material, Materials Science in Semiconductor Processing. 30 (2015) 157–161. https://doi.org/https://doi.org/10.1016/j.mssp.2014.09.047.

[40] K. Gholami Laelabadi, R. Moradian, I. Manouchehri, One-Step Fabrication of Flexible, Cost/Time Effective, and High Energy Storage Reduced Graphene Oxide@PANI Supercapacitor, ACS Applied Energy Materials. 3 (2020) 5301–5312. https://doi.org/10.1021/acsaem.0c00317.

[41] W. Ndambakuwa, Y. Ndambakuwa, J. Choi, G. Fernando, D. Neupane, S.R. Mishra, F. Perez, R.K. Gupta, Nanostructured nickel-cobalt oxide and sulfide for applications in supercapacitors and green energy production using waste water, Surface and Coatings Technology. 410 (2021). https://doi.org/10.1016/j.surfcoat.2021.126933.

[42] Y. Fan, H. Chen, Y. Li, D. Cui, Z. Fan, C. Xue, PANI-Co3O4 with excellent specific capacitance as an electrode for supercapacitors, Ceramics

International. 47 (2021) 8433–8440. https://doi.org/10.1016/j.ceramint.2020.11.208.

[43] X. Zhang, X. Meng, Q. Wang, B. Qin, L. Jin, Q. Cao, Preparation and electrochemical investigation of polyaniline nanowires for high performance supercapacitor, Materials Letters. 217 (2018) 312–315. https://doi.org/10.1016/j.matlet.2018.01.112.

[44] C. Wu, Y. Zhu, C. Guan, C. Jia, W. Qin, X. Wang, K. Zhang, Mesoporous aluminium manganese cobalt oxide with pentahedron structures for energy storage devices, Journal of Materials Chemistry A. 7 (2019) 18417–18427. https://doi.org/10.1039/c9ta06319f.

[45] J. Li, N. Jiang, J. Liao, Y. Feng, Q. Liu, H. Li, Nonstoichiometric Cu0.6Ni0.4Co2O4 nanowires as an anode material for high performance Lithium storage, Nanomaterials. 10 (2020). https://doi.org/10.3390/nano10020191.

[46] R.K. Gupta, J. Candler, S. Palchoudhury, K. Ramasamy, B.K. Gupta, Flexible and High Performance Supercapacitors Based on NiCo2O4 for Wide Temperature Range Applications, Scientific Reports. 5 (2015). https://doi.org/10.1038/srep15265.

[47] S. Sahoo, S. Zhang, J.J. Shim, Porous Ternary High Performance Supercapacitor Electrode Based on Reduced graphene oxide, NiMn2O4, and Polyaniline, Electrochimica Acta. 216 (2016) 386–396. https://doi.org/10.1016/j.electacta.2016.09.030.

[48] M. He, L. Cao, W. Li, X. Chang, X. Zheng, Z. Ren, NiO nanoflakes decorated needle-like MnCo2O4 hierarchical structure on nickle foam as an additive-free and high performance supercapacitor electrode, Journal of Materials Science. 56 (2021) 8613–8626. https://doi.org/10.1007/s10853-021-05810-8.

[49] Y. Zhu, H.C. Chen, C.S. Hsu, T.S. Lin, C.J. Chang, S.C. Chang, L.D. Tsai, H.M. Chen, Operando unraveling of the structural and chemical stability of P-substituted CoSe 2 electrocatalysts toward hydrogen and oxygen evolution reactions in alkaline electrolyte, ACS Energy Letters. 4 (2019) 987–994. https://doi.org/10.1021/acsenergylett.9b00382.

[50] M.P. Mani, V. Venkatachalam, K. Thamizharasan, M. Jothibas, Evaluation of Cubic-Like Advanced ZnMn2O4 Electrode for High-Performance Supercapacitor Applications, Journal of Electronic Materials. 50 (2021) 4381–4387. https://doi.org/10.1007/s11664-021-08962-0.

[51] H. Fan, H. Yu, Y. Zhang, Y. Zheng, Y. Luo, Z. Dai, B. Li, Y. Zong, Q. Yan, Fe-Doped Ni3C Nanodots in N-Doped Carbon Nanosheets for Efficient Hydrogen-Evolution and Oxygen-Evolution Electrocatalysis, Angewandte Chemie - International Edition. 56 (2017) 12566–12570. https://doi.org/10.1002/anie.201706610.

[52] W. Zhou, D. Huang, Y. Wu, J. Zhao, T. Wu, J. Zhang, D. Li, C. Sun, P. Feng, X. Bu, Stable Hierarchical Bimetal–Organic Nanostructures as HighPerformance Electrocatalysts for the Oxygen Evolution Reaction, Angewandte Chemie. 131 (2019) 4271–4275. https://doi.org/10.1002/ange.201813634.

[53] W. Ndambakuwa, Y. Ndambakuwa, J. Choi, G. Fernando, D. Neupane, S.R. Mishra, F. Perez, R.K. Gupta, Nanostructured nickel-cobalt oxide and sulfide for applications in supercapacitors and green energy production using waste water, Surface and Coatings Technology. 410 (2021). https://doi.org/10.1016/j.surfcoat.2021.126933.

[54] H. Wei, J. Zhu, S. Wu, S. Wei, Z. Guo, Electrochromic polyaniline/graphite oxide nanocomposites with endured electrochemical energy storage, Polymer (Guildf). 54 (2013) 1820–1831. https://doi.org/https://doi.org/10.1016/j.polymer.2013.01.051.

[55] J. Ren, W. Bai, G. Guan, Y. Zhang, H. Peng, Flexible and weaveable capacitor wire based on a carbon nanocomposite fiber, Advanced Materials. 25 (2013) 5965–5970. https://doi.org/10.1002/adma.201302498.

[56] D. Guragain, R. Bhattarai, J. Choi, W. Lin, R.K. Gupta, X. Shen, F.A. Perez, S.R. Mishra, Electrochemical performance of aluminum doped ni1−x alx co2 o4 hierarchical nanostructure: Experimental and theoretical study, Processes. 9 (2021). https://doi.org/10.3390/pr9101750.

[57] J. Choi, T. Ingsel, D. Neupane, S.R. Mishra, A. Kumar, R.K. Gupta, Metal-organic framework-derived cobalt oxide and sulfide having nanoflowers architecture for efficient energy conversion and storage, Journal of Energy Storage. 50 (2022) 104145. https://doi.org/10.1016/j.est.2022.104145.

[58] B. Liu, L. Zhang, P. Qi, M. Zhu, G. Wang, Y. Ma, X. Guo, H. Chen, B. Zhang, Z. Zhao, B. Dai, F. Yu, Nitrogen-doped banana peel-derived porous carbon

foam as binder-free electrode for supercapacitors, Nanomaterials. 6 (2016). https://doi.org/10.3390/nano6010018.

[59] G.A.M. Ali, L.L. Tan, R. Jose, M.M. Yusoff, K.F. Chong, Electrochemical performance studies of MnO2 nanoflowers recovered from spent battery, Materials Research Bulletin. 60 (2014) 5–9. https://doi.org/https://doi.org/10.1016/j.materresbull.2014.08.008.

[60] D. Guragain, C. Zequine, R. Bhattarai, J. Choi, R.K. Gupta, X. Shen, S.R. Mishra, Effect of dopant on the morphology and electrochemical performance of Ni1-xCaxCo2O4 (0 = x = 0.8) oxide hierarchical structures, MRS Advances. 5 (2020) 2487–2494. https://doi.org/10.1557/adv.2020.181.

[61] X.C. Dong, H. Xu, X.W. Wang, Y.X. Huang, M.B. Chan-Park, H. Zhang, L.H. Wang, W. Huang, P. Chen, 3D graphene-cobalt oxide electrode for high-performance supercapacitor and enzymeless glucose detection, ACS Nano. 6 (2012) 3206–3213. https://doi.org/10.1021/nn300097q.

[62] N. Wu, X. Bai, D. Pan, B. Dong, R. Wei, N. Naik, R.R. Patil, Z. Guo, Recent Advances of Asymmetric Supercapacitors, Advanced Materials Interfaces. 8 (2021). https://doi.org/10.1002/admi.202001710.

APPENDICES

APPENDICES A - List of peer-reviewed journal publications

- Ginena Shombe, Malik Dilshad Khan, **Jonghyun Choi**, Ram K. Gupta, Marcin Opallo, Neerish Revaprasadu (2022) "Tuning composition of $CuCo_2S_4$-$NiCo_2S_4$ solid solutions via solvent-less pyrolysis of molecular precursors for efficient supercapacitance and water splitting" RSC advances
- Jacob Som, **Jonghyun Choi**, Honglin Zhang, Nikhil Reddy Mucha, Svitlana Fialkova, Kwadwo Mensah-Darkwa, Jin Suntivich, Ram K. Gupta, Dhananjay Kumar (2022) "Effect of substrate-induced lattice strain on the electrochemical properties of pulsed laser deposited nickel oxide thin film" Materials Science & Engineering B
- **Jonghyun Choi**, Kinsey Morey, Anuj Kumar, Dipesh Neupane, Sanjay R. Mishra, Felio Perez, Ram K. Gupta (2022) "Self-Assembled Cotton-like Copper-Molybdenum Sulfide and Phosphide as a Bifunctional Electrode for Green Energy Storage and Production" Materials Today Chemistry
- **Jonghyun Choi**, Tenzin Ingsel, Dipesh Neupane, Sanjay R. Mishra, Anuj Kumar, Ram K. Gupta (2022) "Metal-Organic Framework-Derived Cobalt Oxide and Sulfide Having Nanoflowers Architecture for Efficient Energy Conversion and Storage" Journal of Energy Storage
- **Jonghyun Choi**, Alfred Nkhama, Anuj Kumar, Sanjay R. Mishra, Felio Perez, Ram K. Gupta (2021) "A Facile Preparation of Sulfur Doped Nickel-Iron Nanostructures with Improved HER and Supercapacitor Performance" International Journal of Hydrogen Energy

- Deepa Guragain, Sunil Karna, **Jonghyun Choi**, Tej Poudel, R. Bhattarai, X Shen, Ram Krishna Gupta, Sanjay R Mishra (2021) "Electrochemical Performance of Iron doped Cobalt Oxide Hierarchical Nanostructure" Processes
- Deepa Guragain, Romakanta Bhattarai, **Jonghyun Choi**, Wang Lin, Ram Krishna Gupta, X Shen, Felio A Perez, Sanjay R Mishra (2021) "Electrochemical Performance of Aluminum doped $Ni_{1-x}Al_xCo_2O_4$ Hierarchical Nanostructure: Experimental and Theoretical Study" Processes
- Ginena Shombe, Shumaila Razzaque, Malik Dilshad Khan, Tebello Nyokong, Philani Mashazi, **Jonghyun Choi**, Sanket Bhoyate, Ram Gupta, Neerish Revaprasadu (2021) "Low temperature scalable synthetic approach enabling high bifunctional electrocatalytic performance of $NiCo_2S_4$ and $CuCo_2S_4$ thiospinels" RSC advances
- Sunil Karnal, Dipesh Neupane, Sanjay R. Mishra, **Jonghyun Choi**, Ram K. Gupta, Priya Karna (2021) "Electrochemical Behavior of S and C Mono-Doped Sodium Tantalate Photocatalysts" Journal of Electronic Materials
- Nyemaga Masanje Malima, Malik Dilshad Khan, **Jonghyun Choi**, Ram K. Gupta, Philani Mashazi, Tebello Nyokong, Neerish Revaprasadu (2021) "Solventless synthesis of nanospinel $Ni_{1-x}Co_xFe_2O_4$ ($0 \leq x \leq 1$) solid solutions for efficient electrochemical water splitting and supercapacitance**"** RSC advances
- Gwaza E. Ayom, Malik D. Khan, Ginena B. Shombe, **Jonghyun Choi**, Ram K. Gupta, Werner E. van Zyl, and Neerish Revaprasadu (2021) "Triphenylphosphine-Assisted Transformation of NiS to Ni_2P through a

Solvent-Less Pyrolysis Route: Synthesis and Electrocatalytic Performance" Inorganic Chemistry

- Kelsey Thompson, **Jonghyun Choi**, Dipesh Neupane, Sanjay R. Mishra, Felio Perez, Ram K. Gupta (2021) "Tuning the electrochemical properties of nanostructured CoMoO4 and NiMoO4 via a facile sulfurization process for overall water splitting and supercapacitors" Surface and Coatings Technology
- **Jonghyun Choi**, Taylor Wixson, Adam Worsley, Surendra Dhungana, Sanjay R. Mishra, Felio Perez, Ram K. Gupta (2021) "Pomegranate: An Eco-Friendly Source for Energy Storage Devices" Surface and Coatings Technology
- Wadzanai Ndambakuwa, Yustinah Ndambakuwa, **Jonghyun Choi**, Ganga Fernando, Dipesh Neupane, Sanjay R. Mishra, Felio Perez, Ram K. Gupta (2021) "Nanostructured nickel-cobalt oxide and sulfide for application in supercapacitors and green energy production using wastewater" Surface and Coatings Technology
- D. Guragain, C. Zequine, R. Bhattarai, **J. Choi**, R. K. Gupta, X. Shen, S. R. Mishra (2020) "Effect of dopant on the morphology and electrochemical performance of $Ni_{1-x}Ca_xCo_2O_4$ ($0 \leq x \leq 0.8$) oxide hierarchical structures" MRS Advances
- Nikhil Reddy Mucha , Jacob Som , **Jonghyun Choi** , Surabhi Shaji, Ram K. Gupta, Harry M. Meyer, Corson L. Cramer, Amy M. Elliot, Dhananjay Kumar (2020) "High-Performance Titanium Oxynitride Thin Films for Electrocatalytic Water Oxidation" ACS Applied Energy Materials
- Ginena Bildard Shombe, Malik Dilshad Khan, Asma M. Alenad, **Jonghyun Choi**, Tenzin Ingsel, Ram K. Gupta, Neerish Revaprasadu (2020) "Unusual

doping induced phase transitions in NiS via solventless synthesis enabling superior bifunctional electrocatalytic activity" Sustainable Energy & Fuels

- Felipe M. de Souza, **Jonghyun Choi**, Sanket Bhoyate, Pawan K. Kahol, Ram K. Gupta (2020) "Expendable Graphite as an Efficient Flame-Retardant for Novel Partial Bio-Based Rigid Polyurethane Foams" C—Journal of Carbon Research
- Kaushik Sarkar, Panupong Jaipan, **Jonghyun Choi**, Talisha Haywood, Duy Tran, Nikhil Reddy Mucha, Sergey Yarmolenko, Onome Scott-Emuakpor, Mannur Sundaresan, Ram K. Gupta, Dhananjay Kumar (2020) "Enhancement in corrosion resistance and vibration damping performance in titanium-by-titanium nitride coating" SN Applied Sciences
- **Jonghyun Choi**, Camila Zequine, Sanket Bhoyate, Wang Lin, Xianglin Li, P. K. Kahol, Ram K. Gupta (2019) "Waste Coffee Management: Deriving High-Performance Supercapacitors Using Nitrogen-Doped Coffee-Derived Carbon" C—Journal of Carbon Research

APPENDICES B - List of book chapters

- (Accepted) **Jonghyun Choi**, Tenzin Ingsel, Ram K. Gupta (2022) "Printable and Flexible Solid-State Batteries" Book: Solid State Batteries: Emerging Materials and Applications - ACS
- (Accepted) Felipe M. de Souza, **Jonghyun Choi**, Ram K. Gupta (2021) "Recent Development in Polymer Nanocomposites for Energy Storage Applications" Book - Elsevier
- (Accepted) **Jonghyun Choi**, Felipe M. de Souza, Ram K. Gupta (2021) "Innovative Strategies for Recycling Used Batteries for Brighter Futures" Book – Nano Technology for Battery Recycling, Remanufacturing, and Reusing Chapter 05- Elsevier
- Alfred Nkhma, Muhammad Rizwan Sulaiman, **Jonghyun Choi**, Ram Krishna Gupta "Biowastes for Energy: An Introduction (2022) Book: Energy from waste: Production and Storage – CRC press
- (Accepted) Felipe M. de Souza, **Jonghyun Choi**, Tenzin Ingsel, Ram K. Gupta (2021) "High-Performance Polyurethanes Foams for Automobile Industry" Book: Nanotechnology in the Automotive Industry Chapter 06 - Elsevier

APPENDICES C - List of conference presentations

- **Jonghyun Choi**, Kinsey Morey, Ram K Gupta (2022) “Copper-molybdenum sulfide and phosphide electrodes for superior energy storage and conversion” 2022 PSU Research Colloquium
- **Jonghyun Choi**, A. Gupta, M.E. Ellis, C.A. Allison, R. Gupta (2022) “Metal-Oxide Frameworks-based Cobalt Oxides as Efficient Electrocatalysts” 2022 PSU Research Colloquium
- **Jonghyun Choi**, C.A. Allison, M.E. Ellis, A. Gupta, R. Gupta (2022) “Effect of calcination on the energy storage capacity metal-organic framework-derived cobalt oxides” 2022 PSU Research Colloquium
- Jacob Som, **Jonghyun Choi**, Svitlana Fialkova, Ram Gupta, Dhananjay Kumar (2022) “Effect of Substrate-Induced Lattice Strain on the Electrochemical Properties of Pulsed Laser Deposited Nickel Oxide Thin Film” Bulletin of the American Physical Society
- Felipe M. de Souza, **Jonghyun Choi**, and Ram K. Gupta (2022) “Bio-Based Rigid Polyurethane Foams Blended with Expendable Graphite as an Eco-Friendly and Efficient Flame-Retardant” ACS Spring 2022
- Panupong Jaipan, Jacob Som, **Jonghyun Choi**, Nafeezuddin Mohammad, Manosi Roy, Austin Reese, Jin Suntivich, Ram K. Gupta, Dhananjay Kumar (2021) “Pseudocapacitive titanium oxynitride nanowires by pulsed-laser

deposition for ultra-high capacitance supercapacitors" 2021 MRS PREM Research Scholars Summit

- S. Chaudhary, P. Kote, **J. Choi**, R. Gupta (2021) "MOF-derived metal oxide as a bifunctional electrocatalyst and electrode for supercapacitor applications" 2021 Midwest Regional Meeting of the ACS
- A. Gupta, C.A. Allison, M.E. Ellis, **J. Choi**, R. Gupta (2021) "Effect of temperature on the electrochemical properties of cobalt-based metal-organic frameworks" 2021 Midwest Regional Meeting of the ACS
- M.E. Ellis, C.A. Allison, A. Gupta, **J. Choi**, R. Gupta (2021) "Highly efficient electrocatalysts based on metal-oxide frameworks-derived cobalt oxides for green energy production" 2021 Midwest Regional Meeting of the ACS
- **Jonghyun Choi**, Kinsey Morey, Ram K Gupta (2021) "Bifunctional CuMoS4 for green Energy Production" 239th ECS Meeting with the 18th International Meeting
- **Jonghyun Choi**, Wadzanai Ndambakuwa, Yustinah Ndambakuwa, Ganga Fernando, Sanjay R Mishra, Felio Perez, Ram K Gupta (2021) "Nanostructured Nickel-Cobalt Oxide and Sulfide for Green Energy Production Using Wastewater" 239th ECS Meeting with the 18th International Meeting
- **Jonghyun Choi**, Tenzin Ingsel, Khamis Siam and Ram Gupta (2021) "Metal-Organic Framework based Cobalt Oxide and Cobalt Sulfide as Efficient Electrocatalysts and High- Performance Supercapacitors" 2021 Virtual MRS Spring Meeting & Exhibit

- **Jonghyun Choi**, Taylor Wixson, and Ram K. Gupta (2021) “Pomegranate: An Eco-Friendly Source for Green Energy Storage Devices” 2021 PSU Virtual Research Colloquium
- Felipe M. de Souza, **J. Choi**, and Ram K. Gupta (2021) “Bio-Based Rigid Polyurethane Foams Made Flame-Retardant after Addition of Aluminum Hypophosphite” 2021 PSU Virtual Research Colloquium
- Tenzin Ingsel, **Jonghyun Choi** (2021) “Cost-effective solutions to energy storage system development” 2021 PSU Virtual Research Colloquium
- Felipe de Souza, **J. Choi**, Ravi Arukula, P. K. Kahol, Ram K. Gupta (2020) “Expandable Graphene as an Effective Flame-Retardant In Bio-Based Rigid Polyurethane Foams" 2020 17th Annual Capitol Graduate Research Summit
- **Jonghyun Choi**, Camila Zequine, Sanket Bhoyate, Wang Lin, Xianglin Li, Pawan Kahol, and Ram Gupta (2019) “Development of High-Performance Supercapacitors using Waste Coffee Powder: Importance of Nitrogen-Doping on Electrochemical Properties” ACS 2019 Midwest Regional Meeting